NAVAL POSTGRADUATE SCHOOL
Monterey, California

THESIS

K142385

A Study of the Sensitivity of the Greenland Sea Acoustic Tomography

by

Kao, Chih-Chung

December 1989

Thesis Advisor: Ching-Sang Chiu
Co-advisor: James H. Miller

Approved for public release; distribution unlimited.

T247926

Unclassified

Security Classification of this page

REPORT DOCUMENTATION PAGE

1a Report Security Classification: Unclassified		1b Restrictive Markings	
2a Security Classification Authority		3 Distribution Availability of Report: Approved for public release; distribution is unlimited.	
2b Declassification/Downgrading Schedule			
4 Performing Organization Report Number(s)		5 Monitoring Organization Report Number(s)	
6a Name of Performing Organization: Naval Postgraduate School	6b Office Symbol (*If Applicable*): 61	7a Name of Monitoring Organization: Naval Postgraduate School	
6c Address (*city, state, and ZIP code*): Monterey, CA 93943-5000		7b Address (*city, state, and ZIP code*): Monterey, CA 93943-5000	
8a Name of Funding/Sponsoring Organization	8b Office Symbol (*If Applicable*)	9 Procurement Instrument Identification Number	
8c Address (*city, state, and ZIP code*)		10 Source of Funding Numbers: Program Element Number / Project No / Task No / Work Unit Accession No	

11 Title (*Include Security Classification*): A STUDY OF THE SENSITIVITY OF THE GREENLAND SEA ACOUSTIC TOMOGRAPHY ARRAY

12 Personal Author(s): Kao, Chih-Chung

13a Type of Report	13b Time Covered	14 Date of Report (*year, month,day*)	15 Page Count
Master's Thesis	From To	December 1989	77

16 Supplementary Notation: The views expressed in this thesis are those of the author and do not reflect the official policy or position of the Department of Defense or the U.S. Government.

17 Cosati Codes			18 Subject Terms (*continue on reverse if necessary and identify by block number*)
Field	Group	Subgroup	Ocean Acoustics, Acoustic Tomography.

19 Abstract (*continue on reverse if necessary and identify by block number*)

An acoustic tomography array consisting of six transceiver moorings was jointly deployed by Woods Hole Oceanographic Institution and Scripps Institution of Oceanography in the Greenland Sea during the second half of 1988. Two of the primary objectives of this thesis are: (1) to set up and test a stochastic 3-D inversion code for the Greenland Sea Acoustic Tomography data analysis; and (2) to evaluate the performance of the acoustic system through resolution and variance analyses. In acoustic tomography, the sound speed perturbation field is estimated from measured acoustic travel time perturbation data. A unique sound speed perturbation estimate can be constructed using the Guass-Markoff theorem. However, the theorem requires the specification of the covariance of the sound speed perturbation field, which is generally not exactly known. Via computer simulation, we examined the sensitivity of the estimate to uncertainty in the sound speed field correlation specified. In addition, we also examined the effects of an increased random experimental noise level and a change in array geometry due to mooring failure on the estimate. The three major results are that: (1) the estimate is less sensitive to a positive uncertainty in correlation length than to a negative uncertainty in an ocean volume containing large structures, while it is more sensitive to a positive uncertainty than to a negative uncertainty in an ocean volume containing small structures; (2) the estimate error is primarily bias error rather than random error; and (3) the failure of a mooring causes a large increase in RMS error in regions no longer containing acoustic rays, but it results in an increase in RMS error of only 25% in regions which still contain acoustic rays.

20 Distribution/Availability of Abstract	21 Abstract Security Classification	
[X] unclassified/unlimited [ ] same as report [ ] DTIC users	Unclassified	
22a Name of Responsible Individual: Ching-Sang Chiu	22b Telephone (*Include Area code*): (408) 646-3239	22c Office Symbol: 68Ci

DD FORM 1473, 84 MAR 83 APR edition may be used until exhausted

All other editions are obsolete

security classification of this page

Unclassified

Approved for public release; distribution is unlimited.

A Study of the Sensitivity of the Greenland Sea Acoustic Tomography Array

by

Kao, Chih-Chung
Lieutenant, TAIWAN NAVY, R.O.C.
B.S., Chung Cheng Institute of Technology, 1982

Submitted in partial fulfillment of the requirements
for the degree of

MASTER OF SCIENCE IN ENGINEERING ACOUSTICS

from the

NAVAL POSTGRADUATE SCHOOL
December 1989

ABSTRACT

An acoustic tomography array consisting of six transceiver moorings was jointly deployed by Woods Hole Oceanographic Institution and Scripps Institution of Oceanography in the Greenland Sea during the second half of 1988. Two of the primary objectives of this thesis are: (1) to set up and test a stochastic 3-D inversion code for the Greenland Sea Acoustic Tomography data analysis; and (2) to evaluate the performance of the acoustic system through resolution and variance analyses. In acoustic tomography, the sound speed perturbation field is estimated from measured acoustic travel time perturbation data. A unique sound speed perturbation estimate can be constructed using the Guass-Markoff theorem. However, the theorem requires the specification of the covariance of the sound speed perturbation field, which is generally not exactly known. Via computer simulation, we examined the sensitivity of the estimate to uncertainty in the sound speed field correlation specified. In addition, we also examined the effects of an increased random experimental noise level and a change in array geometry due to mooring failure on the estimate. The three major results are that: (1) the estimate is less sensitive to a positive uncertainty in correlation length than to a negative uncertainty in an ocean volume containing large structures, while it is more sensitive to a positive uncertainty than to a negative uncertainty in an ocean volume containing small structures; (2) the estimate error is primarily bias error rather than random error; and (3) the failure of a mooring causes a large increase in RMS error in regions no longer containing acoustic rays, but it results in an increase in RMS error of only 25% in regions which still contain acoustic rays.

C.1

TABLE OF CONTENTS

I. INTRODUCTION 1

A. OCEAN ACOUSTIC TOMOGRAPHY 1

B. GREENLAND SEA PROJECT OCEAN ACOUSTIC TOMOGRAPHY 3

C. THESIS OBJECTIVE 6

II. ACOUSTIC FORWARD MODELING 8

A. TRAVEL TIME 8

B ACOUSTIC RAYS IN AN INHOMOGENEOUS MOVING MEDIUM 11

1. Ray Path 12

2. Numerical 4th Order Runge-Kutta Integration Method 15

3. Turning Point 16

4. Surface Reflection 19

5. Eigenrays Finding 21

III. STOCHASTIC INVERSE METHOD 26

A. ESTIMATION OF SOUND SPEED FIELDS 26

1. The Gauss-Markoff Estimator 26

B. ERROR AND RESOLUTION 28

1. Error of the Estimate 28

2. Resolution 29

IV. RESULTS OF SENSITIVITY STUDY 34

A. COMPUTER SIMULATION OF MESOSCALE SOUND SPEED FIELDS AND TRAVEL TIME DATA 35

B. SYSTEM PERFORMANCE 38

1. RMS Error Analysis 38

2. Resolution Analysis 47

C. SENSITIVITY OF INVERSE SOLUTION 53

V. CONCLUSION 61
A. ESTIMATOR PERFORMANCE 61
B. RECOMMENDATIONS FOR FUTURE IMPROVEMENT 63
REFERENCES 64
INITIAL DISTRIBUTION LIST 66

LIST OF NOTATION

T	Acoustic travel time
c	Sound speed
$\tilde{\mathbf{v}}$	Ocean current velocity
$\hat{\tau}$	Unit vector tangent to ray path
c_o	Reference sound speed
δc	Sound speed perturbation
T_o	Reference travel time
δT	Travel time perturbation
$\mathbf{r}$	Position vector, $\mathbf{r} = (x,y,z)$
t	Time
s	Arc length of acoustic ray path
$\mathbf{A}$	Matrix of forward transfer function ($n \times m$)
A_{ij}	ith row, jth column element in $\mathbf{A}$
i	Travel time data index, $i = 1, 2, \ldots\ldots, m$
j	Ocean box index, $j = 1, 2, \ldots\ldots, n$
Φ	Eikonal function
n	Index of refraction
$\mathbf{v}$	Nondimensional ocean current velocity vector, $\mathbf{v} = \tilde{\mathbf{v}}/c$
v	Magnitude of $\mathbf{v}$
R	Range

LIST OF NOTATION (CONTINUED)

$\hat{R}$ and $\hat{z}$	Unit vector in R and z direction, respectively
θ	Ray angle
h	Step size in range
ξ	Root of local maximum value of the fourth derivative
κ	Curvature of acoustic ray path
$\mathcal{R}$	Radius of curvature
g_c, g_v	Sound speed gradient, ocean current speed gradient
Z	Depth
$\underline{\delta T}$	Vector of Travel time data (m×1)
$\underline{\delta c}$	Vector of sound speed perturbation (n×1)
$\underline{\hat{\delta c}}$	Vector of sound speed perturbation estimate (n×1)
$\underline{\varepsilon}$	Vector of estimate error (n×1)
$\underline{e}$	Vector of random noise (m×1)
$\mathbf{C}_{\underline{\delta c}}$	Covariance matrix of sound speed perturbation (n×n)
$\mathbf{C}_{\underline{e}}$	Covariance matrix of random noise (n×n)
$\mathbf{C}_{\underline{\varepsilon}}$	Covariance matrix of estimate error (n×n)
$\langle \mathbf{b}\mathbf{b}^T \rangle$	Covariance matrix of bias error in the estimate (n×n)
$\mathbf{C}_{\Delta(\underline{\delta c})}$	Covariance matrix of random error in the estimate (n×n)
$\sigma^2_{\underline{\delta c}}$	Variance of sound speed perturbation

LIST OF NOTATION (CONTINUED)

$\sigma_{\underline{e}}^2$	Variance of random noise
U, **V**	The left singular matrix (m×m) and right singular matrix (n×n) in a singular value decomposition
$\underline{u}_i$, $\underline{v}_j$	*i*th and *j*th columns of **U** and **V**, respectively
Λ, λ_i	Matrix (m×n) containing singular values and the *i*th diagonal element (singular value), respectively
L_x,L_y	Horizontal correlation lengths of sound speed perturbation field in the x and y directions, respectively
L_z	Vertical correlation length of sound speed perturbation field
$\mathcal{H}_x$, $\mathcal{H}_y$	Minimum horizontal resolution lengths
$\mathcal{V}$	Minimum vertical resolution length
R, $\underline{r}_i^T$	Resolution matrix (n×n) and the *i*th resolution kernel vector (n×1), respectively
E_i	The total energy of the *i*th resolution kernel $\underline{r}_i^T$
σ_E	Square root of spatial average of mean square error
σ_ξ	Square root of spatial average of square error

ACKNOWLEDGEMENTS

I would like to thank my thesis advisors Dr. Ching-Sang Chiu and Dr. James H. Miller for their excellent guidance, constant motivation and patience from the very beginning through all my thesis work. I also especially thank them for providing such an interesting topic and user-friendly consulting.

I am very grateful for the strong encouragement and support from my prior supervisor, Dr. Yao, at the Naval Hydrographic and Oceanographic Office, R.O.C. His effort in requesting approval for my education at the Naval Postgraduate School allow me to accomplish this research.

I sincerely thank Mr. David Pierce and Mr. Don Smith who read my preliminary draft and gave valuable suggestions and English help. I also thank Donna Burych, Craig Motell, Russ Schwanz, Laura Ehret, and Sönke Paulsen for computer help since they have kindly helped even when I interrupted their jobs with my computer questions. I thank Mike Weisskopf for his help in thesis format and typing, and I thank Rod Scott for his helpful advice in ray trace programming.

Also I wish to show my appreciation to CDR Kurt V. Schnebele for his very early help with the Transverse Mercator code, which enabled me to start my thesis work.

I am indebted to Mr. Bob Dees for an enriching exposure to the American way of life. He was a great sponsor and is a good friend.

Finally, I thank my father for his long term effort and love for me and my family.

I. INTRODUCTION

A. OCEAN ACOUSTIC TOMOGRAPHY

Ocean Acoustic Tomography is a method used to monitor the mesoscale ocean variability (which is the oceanic analog of atmospheric weather) and it was introduced by Munk and Wunsch (1979). This technique is analogous to the medical X-ray procedure known as Computer Assisted Tomography (CAT) (Figure 1-1.a). Roughly speaking, tomography exploits the fact that the ocean is "transparent" to acoustic rays to remotely sense the properties of an ocean region.

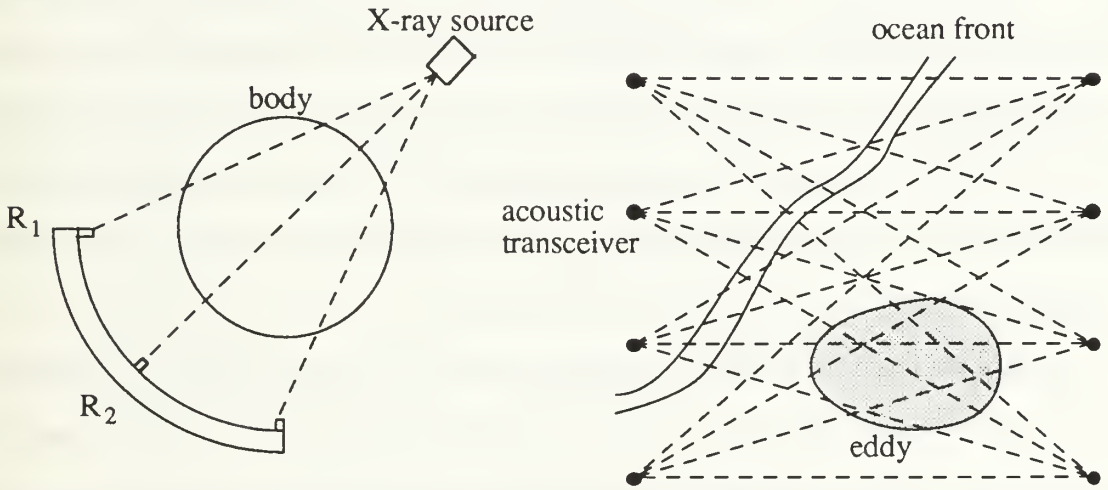

(a) Medical CAT (b) Ocean Acoustic Tomography

Figure 1-1: The Comparison of Medical CAT and Ocean Acoustic Tomography.

In practice, a number of acoustic transceivers are deployed at positions chosen to allow for coverage of an ocean volume of interest (such as a region containing mesoscale eddies or a frontal system) (Figure 1-1.b). The most common

application of tomography is for estimating the perturbation of the sound speed field from a set of measured acoustic travel time perturbations. The perturbations in sound speed are assumed to be so small that the perturbations in acoustic travel time between each pair of transceivers are linearly related to the sound speed perturbations. The modeling of the travel time perturbations due to the sound speed perturbations is known as the *forward problem*. Once the forward problem is solved, inverse methods which are widely used in geophysical research (Backus and Gilbert, 1967) are applied to the travel time data for the reconstruction of the the sound speed perturbation field.

Ocean Acoustic Tomography offers several advantages over conventional hydrographic surveying method. These advantages are pointed out by Chiu (1978): (1) the system can be implanted in the ocean on a semipermanent basis to allow for continuous observation; (2) it is not affected greatly by weather conditions; (3) it has high temporal resolution; (4) it can cover an extensive volume of the ocean interior and probe the different parts simultaneously; and (5) only a few moorings are needed, thus minimizing the effort in deployment and maintenance.

Since the first successful experiment (the 1981 Three-dimensional Mesoscale Experiment), additional tomography projects have provided measurements of mesoscale eddies (Cornuelle *et al*, 1983), planetary waves (Chiu *et al*, 1987), currents (DeFerrari *et al*, 1986), internal waves (Stoughton *et al*, 1986), basin mode oscillations (Bushong, 1987), and surface waves (Lynch *et al*, 1987). In the future, monitoring of large-scale ocean dynamics on a global basis may be achieved using cross-basin transmissions.

B. GREENLAND SEA PROJECT OCEAN ACOUSTIC TOMOGRAPHY

The Greenland Sea Project (GSP) is a plan developed by the international Greenland Sea Science Planning Group which was appointed by the Arctic Ocean Sciences Board (AOSB). The overall goal of this five-year program (from 1987 to 1992) defined by AOSB is to understand the large scale, long-term interactions among the air, sea, and ice in the Greenland Sea. The primary region of the study is bounded by Fram Strait to the north, Spitsbergen and the Mohn Rise to the east, the Greenland-Jan Mayen Ridge to the south, and Greenland to the west (Greenland Sea Science Planning Group, 1986, pp. 1-7).

The plan is designed to study the following ocean dynamics: (1) the seasonal and interannual variability of the sea ice cover; (2) ocean ventilation and convection of the deep water; (3) ocean circulation and mixing; (4) atmosphere energetics; and (5) biological processes. The Ocean Acoustic Tomography Array is a component used in GSP to monitor the process of ocean ventilation and convection in the Greenland sea central gyre (Greenland Sea Science Planning Group, 1986, pp. 1-7). It is the process of ventilation and convection that gives the Greenland Sea central gyre the ability to affect the oceans throughout the world.

An acoustic tomography array consisting of six transceiver moorings with a pentagonal geometry was jointly deployed by Woods Hole Oceanographic Institution and Scripps Institution of Oceanography in the Greenland Sea during the second half of 1988. Figure 1-2 shows the tomography array position and the GSP area.

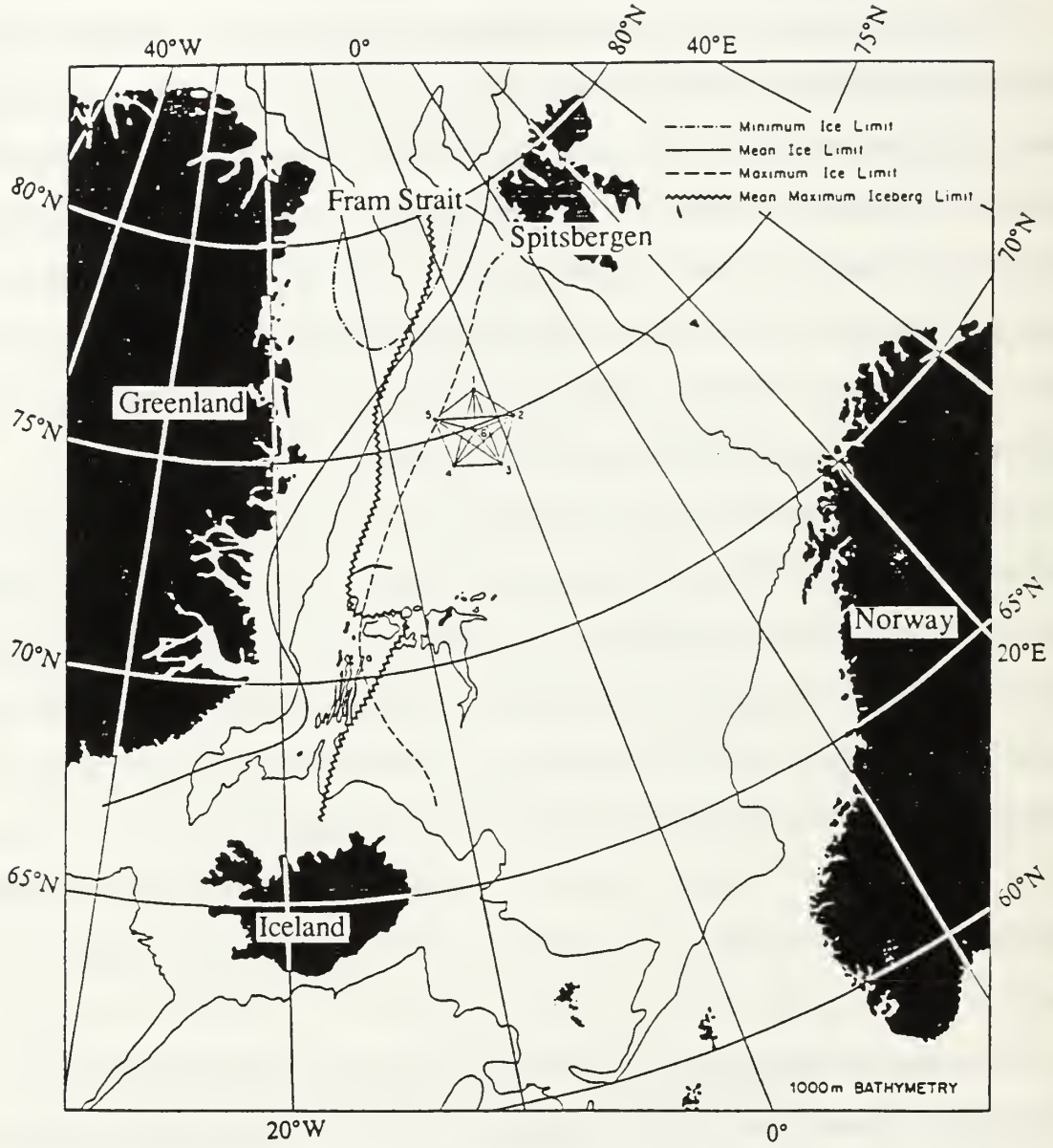

Figure 1-2: Acoustic Tomography Mooring Array Position and Geometry Configuration.

For convenience of calculation, the given geodetic position (latitude and longitude) of each array element has been translated into an xy position using a Transverse Mercator (TM) projection. To do this, the longitude of the central mooring (array #6), was chosen as the central meridian of the TM projection. The false origin was set at 73°N and shifted to 120 km west of the central meridian. This coordinate system gives only slight position distortion at the edge of the array. The ray paths can then be calculated in the xy planar coordinates rather than in geodetic coordinates. TABLE 1-1 shows the coordinate conversion for the moorings as well as the depths of the acoustic sources and vertical receiver arrays.

TABLE 1-1: COORDINATE CONVERSION OF THE ACOUSTIC MOORINGS (USING WGS72 SPHEROID)

Mooring	Lat.	Lon.	x (meter)	y (meter)	S-depth* (meter)	R-depth** (meter)
1	75°47.9'N	1°04.7'W	150726	312598	94.5	145.3
2	74°53.3'N	1°24.8'E	225124	213940	95.0	145.4
3	74°00.4'N	1°05.2'W	154249	112659	94.6	145.1
4	74°18.9'N	4°59.0'W	36008	148715	94.6	117.0
5	75°25.2'N	5°15.9'W	33882	272309	94.8	117.7
6	74°54.0'N	2°12.0'W	120000	212040	95.2	145.7

* The depth of acoustic source.

** The depth of vertical acoustic receiver array.

C. THESIS OBJECTIVE

The purpose of this research is to develop computational tools in preparation for analysis of the tomography data from the GSP. Specifically, our objectives are:

- to set up and test a stochastic 3-D inversion code for the Greenland Sea Acoustic Tomography data analysis; and
- to investigate the sensitivity of the sound speed perturbation estimate to our uncertainty in the sound speed field correlation, changes in the random experimental noise level, and changes in array geometry due to mooring failure. The second objective is accomplished via computer simulation.

In Chapter II, we discuss the behavior of an acoustic ray in an inhomogeneous moving medium. A linear sound speed profile is taken as the reference state of the sound speed field. Based on this reference state, a numerical 4th order Runge-Kutta integration method was used to calculate the paths of the eigenrays for establishing the forward acoustic model. We then discretize the forward model by dividing the ocean volume into 500 boxes in order to cast the problem into a matrix form for the computer simulation.

In Chapter III we present a three-dimensional stochastic inverse method which is the *distribution-free* Gauss-Markoff estimator. Due to insufficient experiment data, the inverse problem is underdetermined. In this stochastic approach, *a priori* information is specified in the covariance matrix of sound speed perturbations. The covariance gives additional constraints to the system and therefore a unique solution is obtained. Two measures, RMS error and resolution length, are used to quantify the performance of the estimator at each box location.

The ocean is a dynamic and inhomogeneous environment. It is difficult to incorporate an exact sound speed perturbation covariance matrix as a constraint since we do not have enough statistical information at this time. Therefore, an *approximate* sound speed perturbation covariance matrix is generally used. When the covariance is inexact, the estimator is *suboptimal*. In Chapter IV, we vary the assumed correlation length (which is used to construct the sound speed perturbation covariance matrix for the estimator) to determine the sensitivity of the system to uncertainty in correlation length. We also study the effects of experimental random noise and failure of array elements on the estimate on the estimate.

In Chapter V, we present a summary of our research, along with results and conclusions. Furthermore, we propose a criterion for designing estimators for the analysis of the GSP data. Finally, we make recommendations for improving our research.

II. ACOUSTIC FORWARD MODELING

A. TRAVEL TIME

In acoustic tomography, the sound speed and flow fields are reconstructed from travel time measurements. The corresponding forward problem is, therefore, to find eigenrays, i.e., those rays which emitted by the source that are intercepted by the receiver, and to establish the relation between the measurement and the unknown fields. Each eigenray has a unique launch angle, and a unique path through the ocean, thereby sampling the sound speed field and flow field, at different locations (Cornuelle, 1983, pp. 41).

The geometric approximate travel time along a ray path, T(t), can be calculated by integrating the ray slowness along the path. In the presence of a current $\tilde{\mathbf{v}}(\mathbf{r},t)$, T(t) is given by

$$T(t) = \int_{Path} \frac{ds}{c(\mathbf{r},t) + \tilde{\mathbf{v}}(\mathbf{r},t) \cdot \hat{\tau}}, \tag{2.1}$$

where $c(\mathbf{r},t)$ is the sound speed at time t and position $\mathbf{r}$, $\tilde{\mathbf{v}}(\mathbf{r},t)$ is the ocean current velocity, $\hat{\tau}$ is a unit vector tangent to the ray, and s is the arc length along the path. The travel time is changed by the sound speed perturbation field, $\delta c(\mathbf{r},t)$, which is the deviation from the reference sound speed, $c_o(\mathbf{r})$. The reference sound speed can be the overall space-time average sound speed. Thus the travel times in a reciprocal transmission can be expressed as

$$T^f = T_o + \delta T^f = \int_{path} \frac{ds}{c_o(\mathbf{r},t) + \delta c(\mathbf{r},t) + \tilde{\mathbf{v}}(\mathbf{r},t) \cdot \hat{\tau}} \tag{2.2}$$

and

$$T^b = T_o + \delta T^b = \int_{path} \frac{ds}{c_o(\mathbf{r},t) + \delta c(\mathbf{r},t) - \tilde{\mathbf{v}}(\mathbf{r},t) \cdot \hat{\tau}}, \tag{2.3}$$

where the superscripts f and b refer to forward and backward transmissions, respectively, and δT is the perturbation of the reference travel time T_o.

In most ocean environments, $\delta c/c_o$ is on the order of 10^{-2}. Thus we can approximately linearize the reciprocal travel time perturbations as

$$\delta T^f = - \int_{path} \frac{\left[\delta c(\mathbf{r},t) + \tilde{\mathbf{v}}(\mathbf{r},t) \cdot \hat{\tau}\right]}{c_o^2(\mathbf{r})} ds \tag{2.4}$$

and

$$\delta T^b = - \int_{path} \frac{\left[\delta c(\mathbf{r},t) - \tilde{\mathbf{v}}(\mathbf{r},t) \cdot \hat{\tau}\right]}{c_o^2(\mathbf{r})} ds. \tag{2.5}$$

Taking the sum of Eq. (2.4) and Eq. (2.5), one obtains:

$$\delta T^+ = \frac{\delta T^f + \delta T^b}{2} = - \int_{path} \frac{\delta c(\mathbf{r},t)}{c_o^2(\mathbf{r})} ds, \tag{2.6}$$

while taking the difference of Eqs. (2.4) and (2.5), one obtains:

$$\delta T^{-} = \frac{\delta T^{f} - \delta T^{b}}{2} = -\int_{path} \frac{\tilde{v}(r,t) \cdot \hat{\tau}}{c_o^2(r)} ds, \tag{2.7}$$

where δT^{+}, half of the summation of the forward and backward travel time perturbations, is linearly related to the sound speed, and δT^{-}, half of the difference of the forward and backward travel time perturbations, is linearly related to the current. In this thesis our focus is on the estimation of the sound speed perturbations only, and we won't be dealing with Eq. (2.7) at all.

In order to express the travel time in a vector form the continuous integral in Eq. (2.6) was discretized by dividing the ocean into small boxes, in which the sound speed perturbation was assumed constant. Figure 2-1 shows the horizontal transceiver array configuration and the corresponding box geometry in a horizontal slice.

In this project we discretized the ocean volume by 500 boxes (10×10 squares horizontally and 5 layers vertically); the limitation of computer memory space in the microVAX dictated this decision.

After the discretization of the sound speed perturbation field into a vector $\underline{\delta c}$, the vector $\underline{\delta T}$ containing all the eigenray travel times can be expressed in a matrix-vector form as

$$\underline{\delta T} = \mathbf{A}\, \underline{\delta c}, \tag{2.8}$$

where

$$A_{ij} = \frac{\partial \delta T_i}{\partial \delta c_j} = -\int_j \frac{1}{c_o^2} ds_i \tag{2.9}$$

is the element in the *i*th row and *j*th column of the matrix A and is equal to the integral of $^{-1}/_{c_o^2}$ along a segment of the *i*th acoustic ray path in the *j*th ocean box.

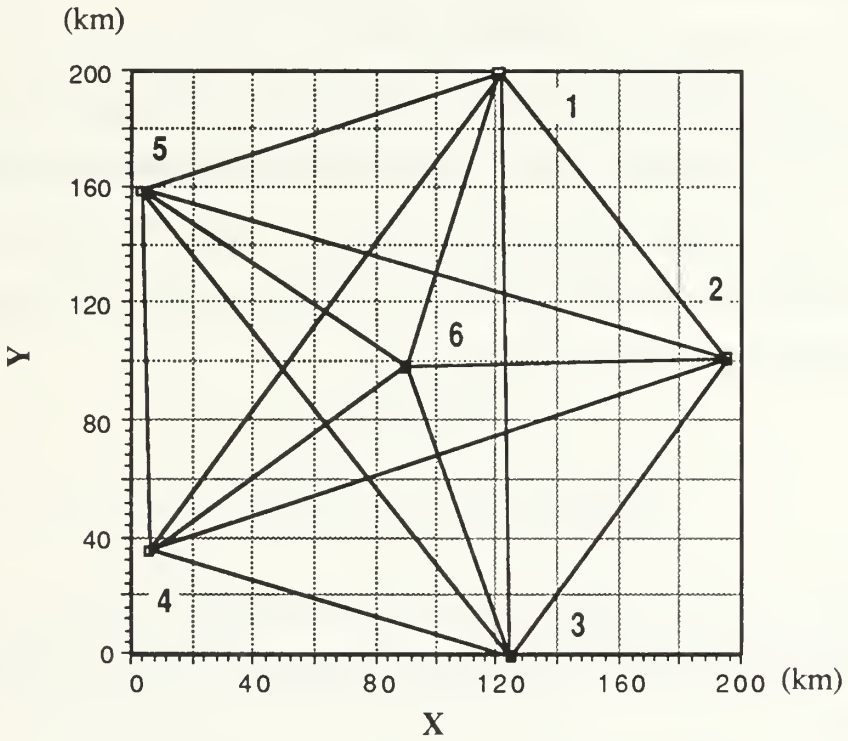

Figure 2.1: The Horizontal Transceiver Array Configuration and the Box Geometry System Used.

B ACOUSTIC RAYS IN AN INHOMOGENEOUS MOVING MEDIUM

A numerical ray-trace algorithm for the acoustic rays in an inhomogeneous moving medium was used in our study. The procedure was developed by Chiu (1985). A summary of the theory will be given in the following discussion.

1. Ray Path

It is well known, in acoustic ray theory, that the acoustic rays in a motionless medium with space dependent index of refraction, $n(\mathbf{r})$, is described by the eikonal equation:

$$\left|\nabla\Phi(\mathbf{r})\right|^2 = n(\mathbf{r})^2, \tag{2.10}$$

where $\Phi(\mathbf{r})$ is the eikonal function (i.e., acoustic phase) defining the wave fronts, $\mathbf{r} = (x,y,z)$ is the position vector, and $\nabla\Phi(\mathbf{r})$ points to the direction of propagation of acoustic field energy. However, when the inhomogeneous medium is moving with a velocity given by $\tilde{\mathbf{v}}$, the governing eikonal equation for acoustic wave fronts becomes (Uginčius, 1970)

$$\left|\nabla\Phi(\mathbf{r})\right|^2 = n(\mathbf{r})^2\left(1 - \tilde{\mathbf{v}} \cdot \frac{\Phi(\mathbf{r})}{c_o}\right)^2. \tag{2.11}$$

Uginčius (1970) has derived a second-order vector differential equation governing the ray paths based on the eikonal equation Eq. (2.11). The equation for ray paths is

$$\frac{d}{ds}(N\mathbf{r}') - (\mathbf{r}''\cdot\nabla')\mathbf{V} + \mathbf{r}'\times(\nabla\times\mathbf{V}) = \nabla N, \tag{2.12}$$

where

$$N = \frac{n}{S} \quad , \quad \mathbf{V} = p\mathbf{v}, \tag{2.13}$$

$$S = \sqrt{1 - v^2 + (\mathbf{r}'\cdot\mathbf{v})^2}, \tag{2.14}$$

and

$$p = \frac{n(S - \mathbf{r}'\cdot\mathbf{v})}{\left(1 - v^2\right)S}, \tag{2.15}$$

and where N and V are functions of both the position $\mathbf{r}$ of a point as well as the ray direction $\mathbf{r}'$ through that point, and $\mathbf{v} = \tilde{\mathbf{v}}/c$ is nondimensional medium velocity and it has a magnitude equal to v. Note that, we have used ' and " to denote the first and second derivatives with respect to s, respectively.

In the ocean, the current velocity is small compared to the speed of sound. Therefore, Eq. (2.12) can be simplified by eliminating the second order terms involving v^2 in N and V so that

$$N \approx n \quad , \quad V \approx n(1 - \mathbf{r}'\cdot\mathbf{v})\mathbf{v} \, , \tag{2.16}$$

and

$$(\mathbf{r}''\cdot\nabla')\mathbf{V} \approx 0. \tag{2.17}$$

By doing so Eq. (2.12) reduces to

$$\frac{d}{ds}(n\mathbf{r}') + \mathbf{r}'\times\left[\nabla\times n(1 - \mathbf{r}'\cdot\mathbf{v})\mathbf{v}\right] = \nabla n. \tag{2.18}$$

By replacing $\mathbf{r}'$ with $d\mathbf{r}/ds$ in Eq. (2.18) we have

$$\frac{d}{ds}\left(n\frac{d\mathbf{r}}{ds}\right) + \frac{d\mathbf{r}}{ds}\times\left[\nabla\times n\left(1 - \frac{d\mathbf{r}}{ds}\cdot\mathbf{v}\right)\mathbf{v}\right] = \nabla n. \tag{2.19}$$

In this thesis we neglected the ray curvature in the horizontal plane and let the reference sound speed profile to be a function of depth z only. This restriction implies that the reference ray paths are confined to lie on vertical slices normal to the xy plane (Ziomek, 1985, pp. 232). In Figure 2-2 a ray path with such a restriction is shown. On a vertical slice (i.e., a Range-Depth Rz plane), the equations governing the planar rays on this plane are

$$\left[\frac{d}{ds}\left(n\frac{dR}{ds}\right) - \frac{d}{ds}(nv_R)\right]\hat{R} = \frac{\partial n}{\partial R}\hat{R} \tag{2.20}$$

and

$$\left[\frac{d}{ds}\left(n\frac{dz}{ds}\right) - \frac{d}{ds}(nv_z)\right]\hat{z} = \frac{\partial n}{\partial z}\hat{z}, \tag{2.21}$$

where $\hat{R}$ and $\hat{z}$ are the unit vector in R and z direction, respectively.

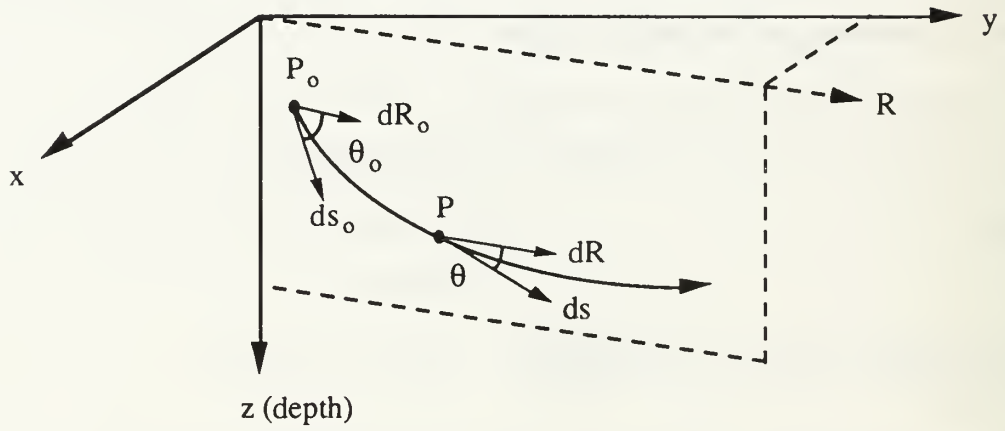

Figure 2-2: The Ray Path Restricted in a Vertical Slice Normal to xy Plane.

Since the reference sound speed profile is taken to be a function of depth only, we can simplify the differential equation (Eq. (2.20)) to get

$$\frac{dR}{ds} = \frac{\cos\theta_o - v_o + n(z)v_R}{n(z)} = \cos(\theta) \tag{2.22}$$

or

$$\frac{dz}{dR} = \pm\sqrt{\left[\frac{n(z)}{\cos\theta_o - v_o + n(z)v_R}\right]^2 - 1} = \tan(\theta). \tag{2.23}$$

where v_o is the medium speed at position (R_o, z_o) in the ray path direction. As shown in Figure 2-2 θ_o and θ are the initial launch angle at position (R_o, z_o) and

ray angle at position (R, z), respectively; Eq. (2.23) can be integrated in either the R or z directions to get the ray paths. In our raytracing we divided each range connecting each of the transceiver pairs in the Greenland Sea into 1,000 steps and integrated Eq. (2.23) in the R direction for the corresponding depth values. Integrating in range gives, for each ray path, depth of the trajectory as a function of range. The function has a one-to-one correspondence.

2. Numerical 4th Order Runge-Kutta Integration Method

An accurate ray path can be calculated using a well known numerical 4th order Runge-Kutta integration method. From Eq. (2.23). the integral for which we need to compute is:

$$z = z_o \pm \int_{R_o}^{R} \sqrt{\left[\frac{n(z)}{\cos\theta_o - v_o + n(z)v_R}\right]^2 - 1}\; dR\,. \tag{2.24}$$

The numerical 4th order Runge-Kutta integration method is given by the following formulae (Gerald, 1989, pp. 358):

$$z_{n+1} = z_n + \int_{R_n}^{R_{n+h}} f\,[R, z(R)]\, dR = z_n + \frac{1}{6}(k_1 + 2k_2 + 2k_3 + k_4)\,, \tag{2.25.1}$$

where

$$f\,[R, z(R)] = \pm \sqrt{\left[\frac{n(z)}{\cos\theta_o - v_o + n(z)v_R}\right]^2 - 1}\;, \tag{2.25.2}$$

$$k_1 = h\, f(R_n\,,\, z_n), \tag{2.25.3}$$

$$k_2 = h\, f(R_n + \tfrac{1}{2}h\,,\, z_n + \tfrac{1}{2}k_1), \tag{2.25.4}$$

$$k_3 = h\, f(R_n + \tfrac{1}{2}h\,,\, z_n + \tfrac{1}{2}k_2), \tag{2.25.5}$$

and

$$k_4 = h\, f(R_n + h\ ,\ z_n + k_3). \qquad (2.25.6)$$

A step size h has been selected to limit the numerical error to a tolerable size. The global error (i.e., discretization error) accumulated along the entire interval R by the 4th order Runge-Kutta method is (Gerald, 1989, pp. 358)

$$O(h^5) = \frac{Rh^4}{180} f^4[\xi, z(\xi)] \quad , \quad 0 < \xi < h. \qquad (2.26)$$

The error cannot be exactly determined because the position (R, z) = [ξ , z(ξ)] is an unknown with ξ bounded by the interval [0, h]. A standard way to determine whether the z values are sufficiently accurate is to compare the value computed using a step size of h with the value calculated using the half of h. If this gives only a change of negligible magnitude, the results are accepted; if not, the step is halved again until the results are satisfactory (Gerald, 1989, pp. 358).

3. Turning Point

As an acoustic ray travels through an ocean volume it will be refracted upward or downward. When the ray angle goes to zero, the ray will start to bend up or down. The position of this zero ray angle point is called the turning point.

When a ray is traced to a position which is less than a step size away from a turning point, we use a linear gradient approximation to calculate the depth of the ray at the terminal of that step. This approximation near a turning point is needed because the function for which we integrate will no longer be the same after the turning point. There will be a sign change in the function. The curvature κ can be used to calculate the ray path around turning point in the linear gradient case. Uginčius (1970) has derived the following equation of curvature:

$$\kappa = \frac{1}{c}\left[\frac{dc}{dz}(v - \frac{dR}{ds}) + \frac{dv}{dz}(2\frac{dR}{ds}v - 1)\right]. \tag{2.27}$$

Let the gradient of sound speed dc/dz be g_c and the gradient of medium speed dv/dz be g_v Eq. (2-27) becomes

$$\kappa = \frac{1}{c}\left[g_c(v - \cos\theta) + g_v(2\cos\theta\, v - 1)\right]. \tag{2.28}$$

Since g_v and v are very small, the term involving the product of g_v and v is negligible. Thus Eq. (2.28) can be approximated by

$$\kappa = \frac{\left[g_c(v - \cos\theta) - g_v\right]}{c}. \tag{2.29}$$

The radius of curvature $\mathcal{R}$ is the reciprocal of κ , i.e.,

$$\mathcal{R} = \frac{c}{\left[g_c(v - \cos\theta) - g_v\right]}. \tag{2.30}$$

Under the assumption of constant gradients near a turning point, the local radius $\mathcal{R}$ is also a constant, which result in a circular ray path, locally. If the radius $\mathcal{R}$ were negative, the radius would curve upward and vice versa (Kinsler, 1982, pp. 401-402). In the following discussion $\mathcal{R}$ will be referred to as the magnitude of the radius of curvature.

The geometries of segments of ray paths through turning points are shown in Figure 2-3 and Figure 2-4, where θ_1 is the ray angle before the turning point and θ_2 is the ray angle after the turning point. The corresponding depth increment can be equated as

$$z_{i+1} - z_i = \pm(\mathcal{R}\cos\theta_2 - \mathcal{R}\cos\theta_1), \tag{2.31}$$

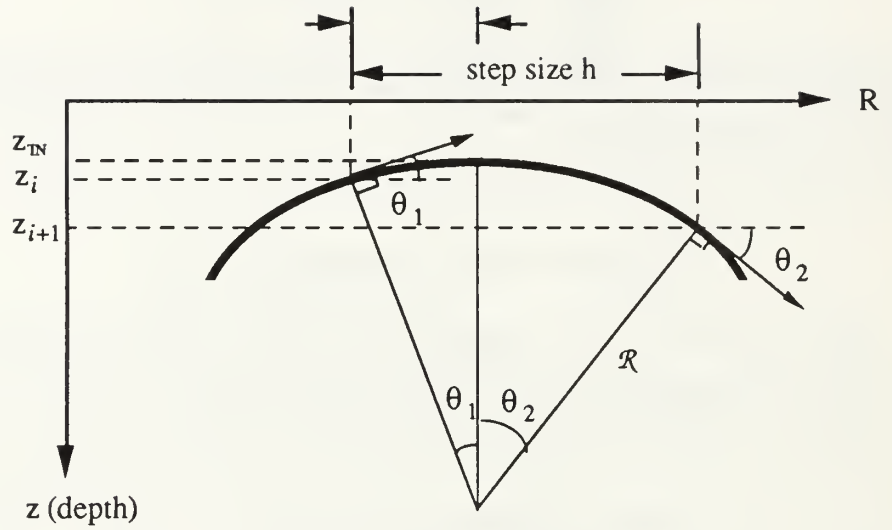

Figure 2-3: The Geometry of a Downward Turning Ray Path.

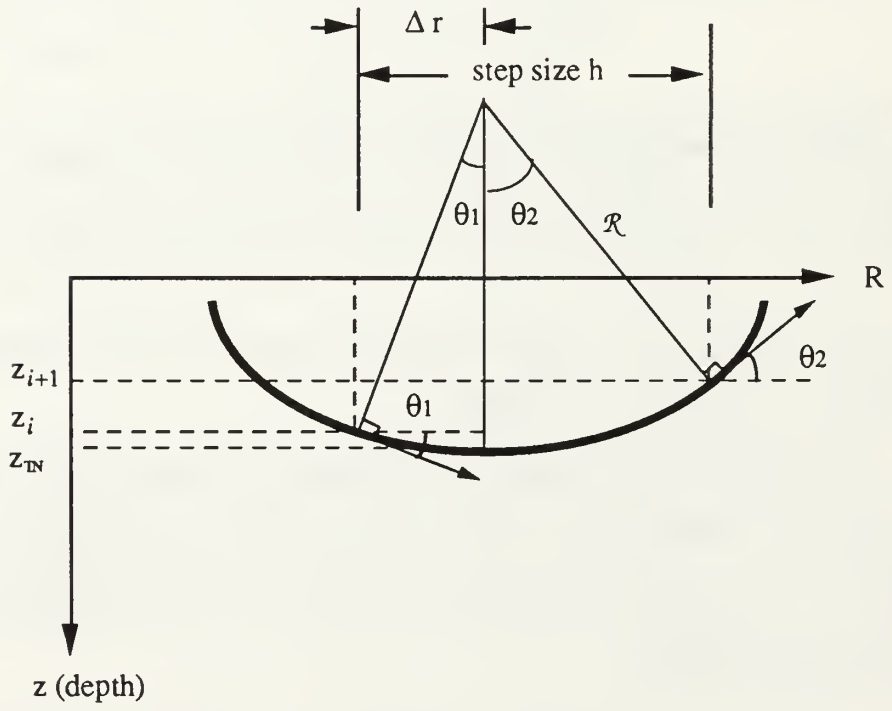

Figure 2-4: The Geometry of an Upward Turning Ray Path.

where

$$\mathcal{R}\cos\theta_2 = \sqrt{\mathcal{R}^2 - (h - \mathcal{R}\sin\theta_1)^2}, \tag{2.32}$$

and "+" is for downward curve while "−" is for upward curve. From Eq. (2.31) the depth of the turning point is simply given by

$$z_{TN} = z_i \pm \mathcal{R}(1 - \cos\theta_1). \tag{2.33}$$

4. Surface Reflection

Due to the upward refracting nature of the Greenland Sea sound channel, surface reflection of rays is of importance. The ray path is discontinuous at the point of reflection and the equation for rays Eq. (2.24) is not valid here. We need to develop a procedure to calculate the local path trajectory near a reflection point in an other way. The same linear gradient assumption, as used for the calculation near a turning point is applicable here again.

Similar to Eq. (2.31), the depth increment in a range step within which a surface reflection occurs is

$$z_{i+1} - z_i = \pm (\mathcal{R}\cos\theta_2 - \mathcal{R}\cos\theta_1). \tag{2.34}$$

In the case of convex path segment (figure 2-5), $\mathcal{R}\cos\theta_2$ is given by

$$\mathcal{R}\cos\theta_2 = \sqrt{\mathcal{R}^2 - (2\mathcal{R}\sin\theta - \mathcal{R}\sin\theta_1 - h)^2} \tag{2.35}$$

and

$$\mathcal{R}\sin\theta = \sqrt{\mathcal{R}^2 - (\mathcal{R}\cos\theta_1 + Z_i)^2}. \tag{2.36}$$

In the case of a concave path segment (Figure 2-6), $\mathcal{R}\cos\theta_2$ is given by

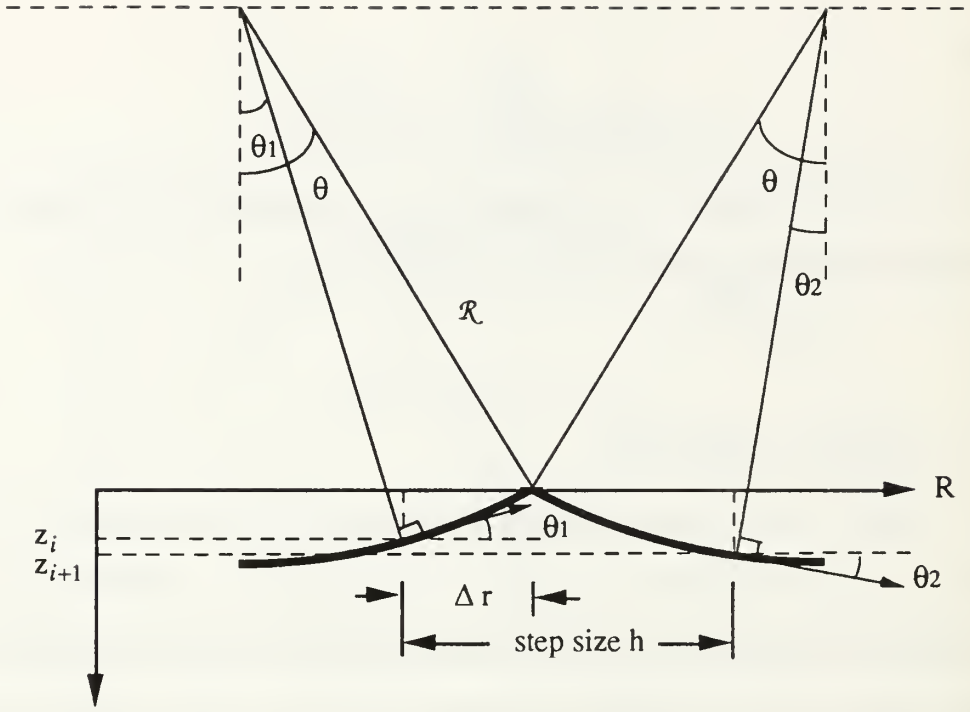

Figure 2-5: The Geometry of a Surface Reflected Convex Path Segment.

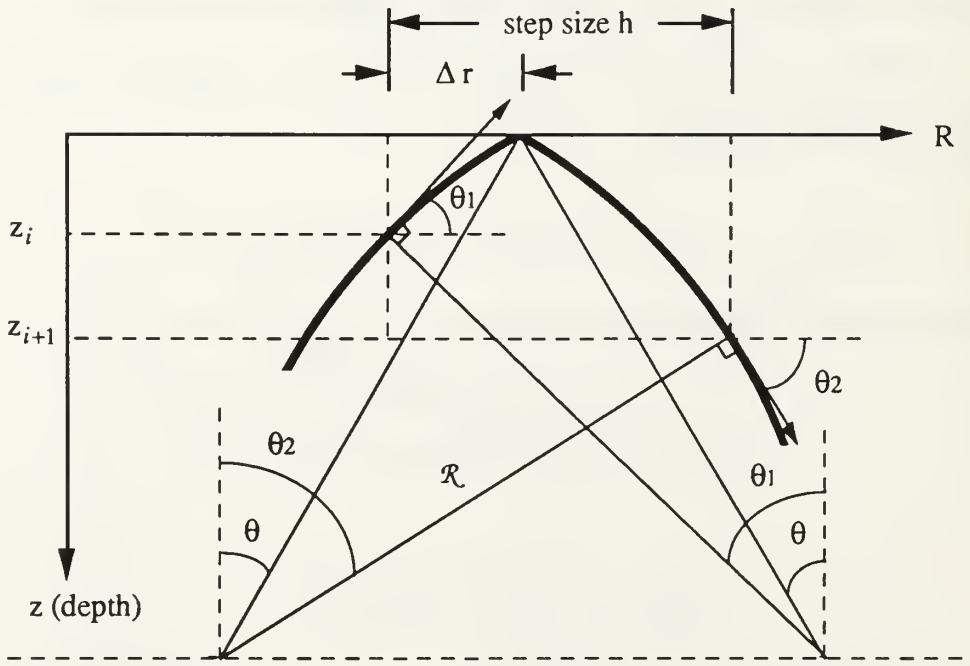

Figure 2-6: The Geometry of a Surface Reflected Concave Path Segment.

$$\mathcal{R}\cos\theta_2 = \sqrt{\mathcal{R}^2 - (2\mathcal{R}\sin\theta - \mathcal{R}\sin\theta_1 + h)^2} \tag{2.37}$$

and

$$\mathcal{R}\sin\theta = \sqrt{\mathcal{R}^2 - (\mathcal{R}\cos\theta_1 - Z_i)^2}\,. \tag{2.38}$$

Having all the equations coded in FORTRAN, predictions of ray paths as well as eigenray finding were possible.

5. Eigenrays Finding

Since the sound-speed profile in the central Greenland Sea gyre is very nearly adiabatic below the surface layers, a linear and range-independent sound speed profile was selected to represent the reference state $c_o(z)$, as shown in Figure 2-7 (left). We then use this reference state to calculate the ray pattern of transmission in the acoustic forward problem.

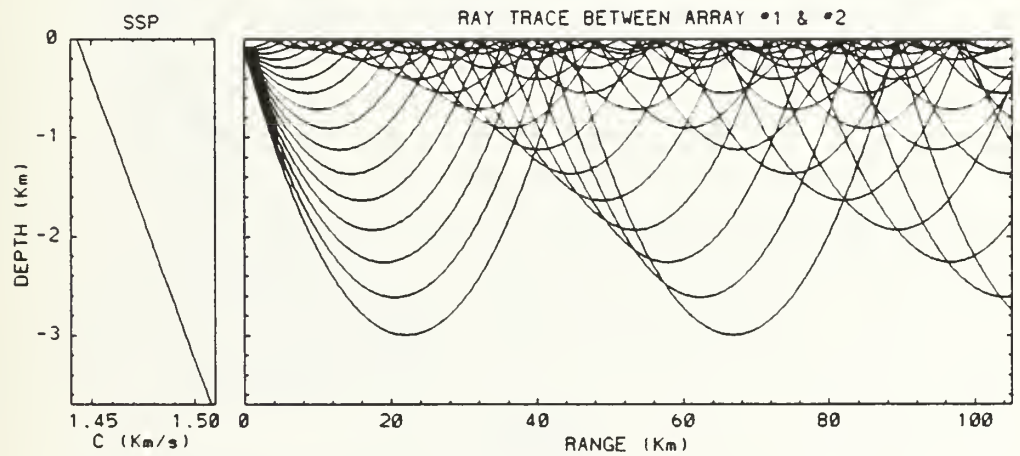

Figure 2-7: Typical Sound Speed Profile and Ray Path with The Ray Angle from -15° to 0° in The Greenland Sea Project Area.

In Figure 2-7 (right) the ray paths shown are the typical propagation pattern in the arctic environment. The rays with fewer loops, that reach the deeper layers, are the faster paths for the acoustic energy.

In order to search for rays that reach the receiver (i.e., eigenrays) we need to shoot rays with a range of launch angles. Given an angular interval within which all possible eigenrays lie, we shall be able to determine the eigenrays by looking for the intersections between the arrival depth curve and the receiver depth line as illustrated in Figure 2-8. Three eigenray patterns associated with 3 different ranges are shown in Figure 2-9. We only choose 6 to 7 out of as many as 30 eigenrays that sample the ocean from the surface to 1 km depth. Figure 2-10 shows the selected eigenrays for the three ranges. There are a total of 91 eigenrays will be used to conduct our sensitivity study.

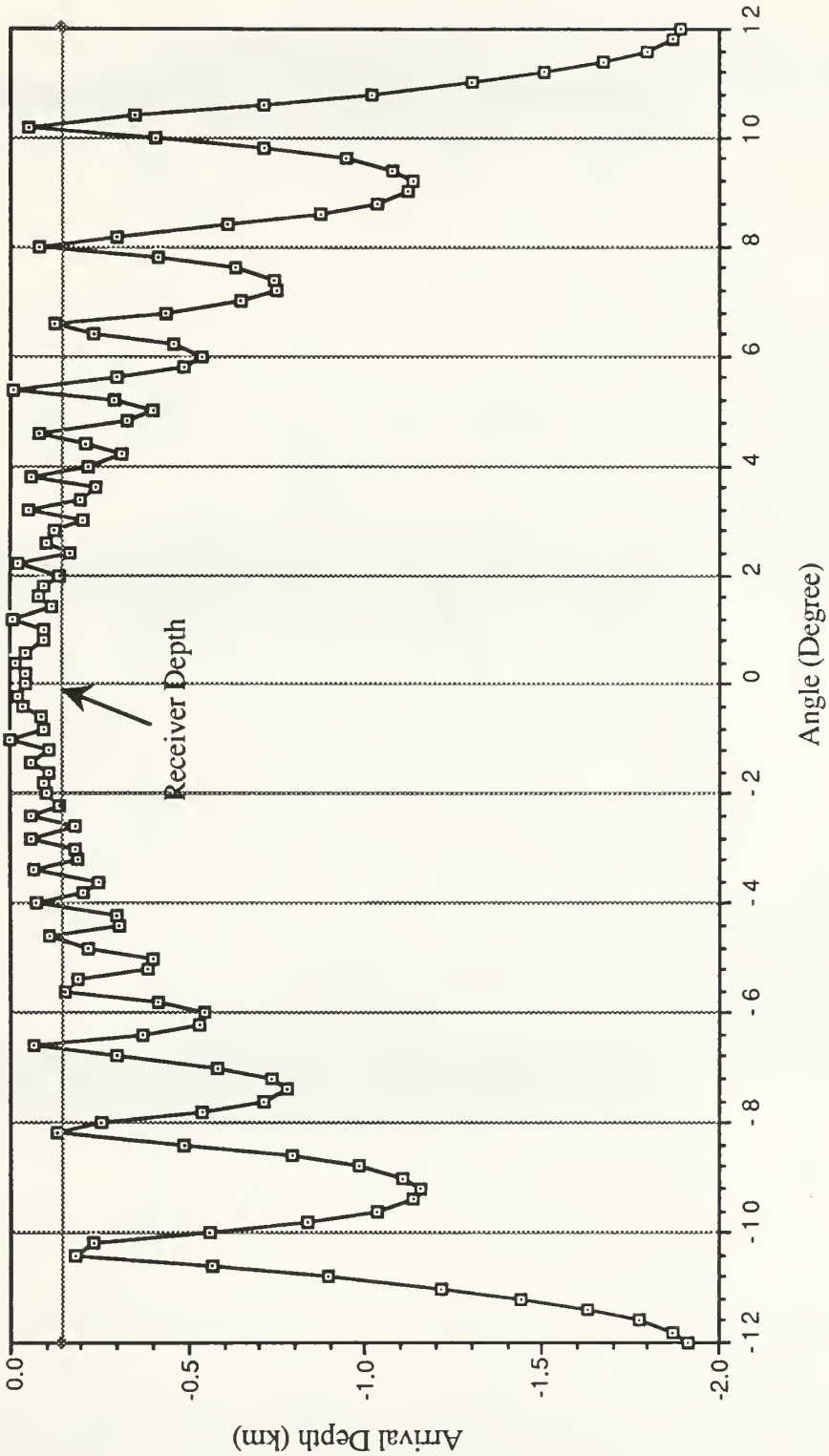

Figure 2-8: Arrival Depth Curve for Eigenrays Finding.

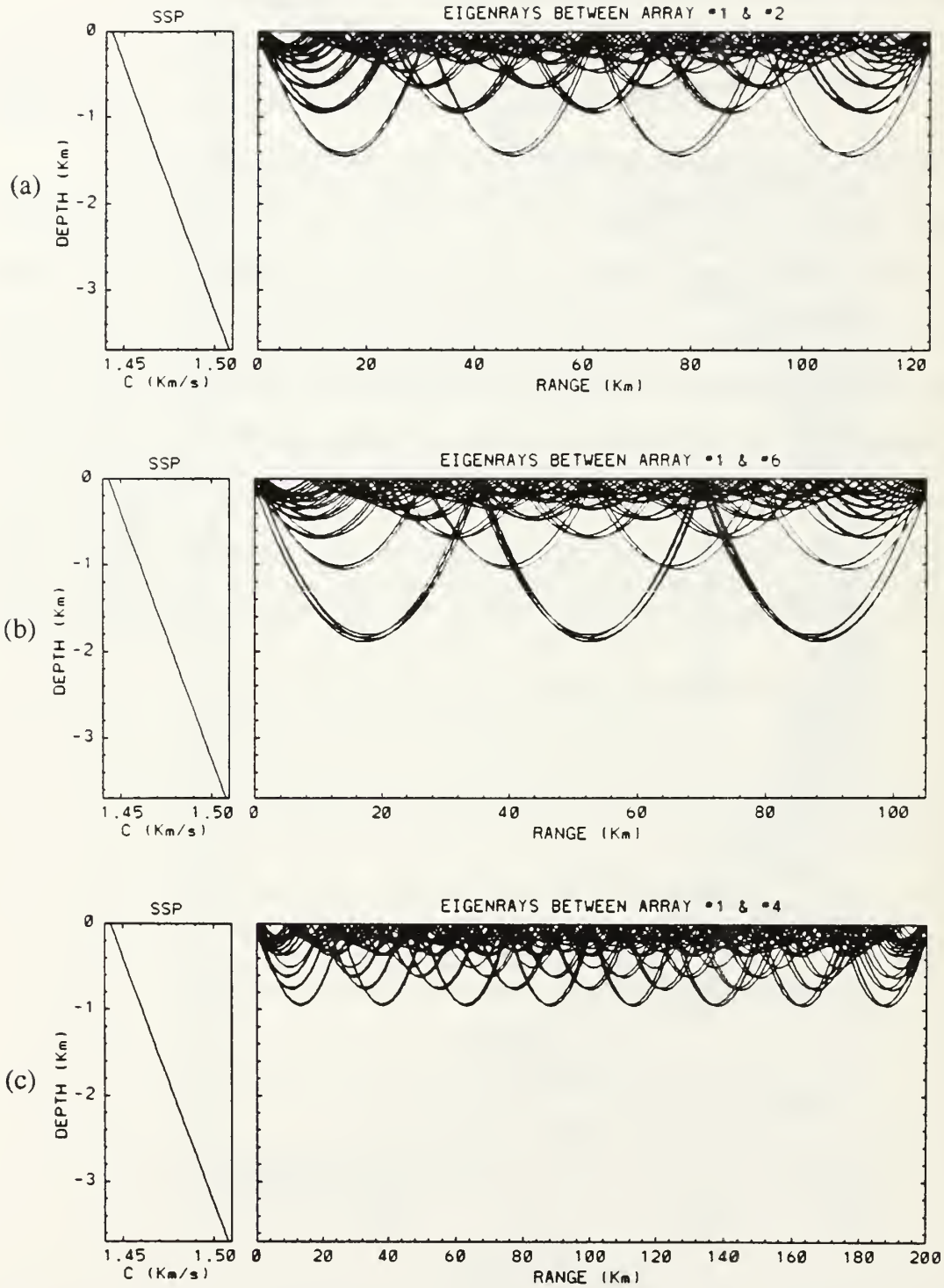

Figure 2-9: Typical Eigenray Pattern for Three Different Range as in (a) Range = 123.6 km, (b) Range = 105.2 km, and (c) Range = 200.1 km.

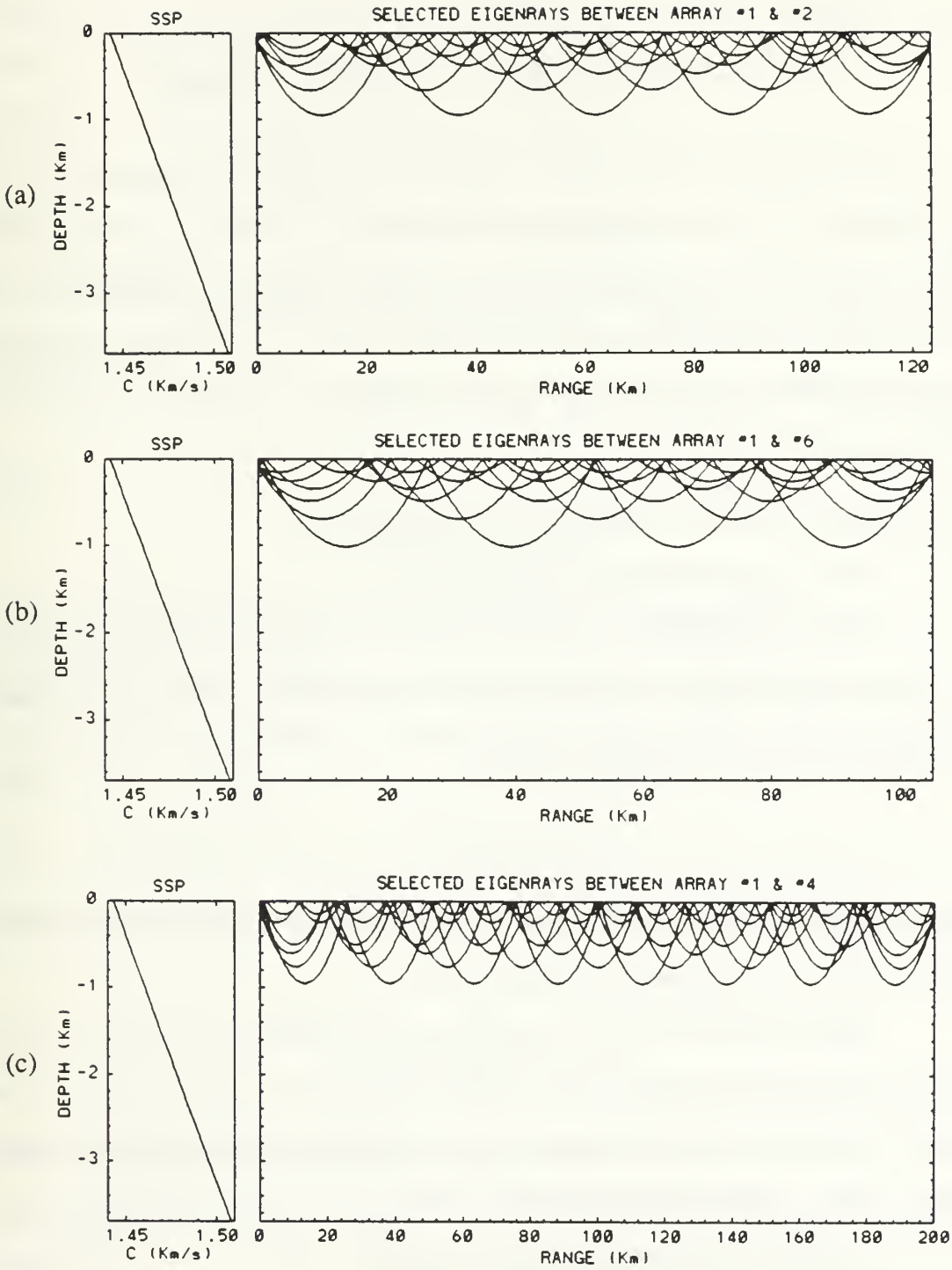

Figure 2-10: Typical Selected Eigenray Pattern for Three Different Range as in (a) Range = 123.6 km, (b) Range = 105.2 km, and (c) Range = 200.1 km.

III. STOCHASTIC INVERSE METHOD

In the forward problem the ray travel times are modeled using Eq. (2.9). In this chapter, we discuss the inversion of Eq. (2.9) using a Gauss-Markoff estimator to obtain an optimal estimate of the three dimensional sound speed field in the ocean volume monitored by the acoustic array. The estimation error and system resolution will be analyzed in the next chapter in an effort to quantify the performance of the array.

A. ESTIMATION OF SOUND SPEED FIELDS.

1. The Gauss-Markoff Estimator

In the Gauss-Markoff stochastic inverse method, both the data $\underline{\delta T}$ and the unknown field $\underline{\delta c}$ are assumed to be random vectors. The forward model relating the data and the unknown field is

$$\underline{\delta T} = \mathbf{A}\, \underline{\delta c} + \underline{e}, \tag{3.1}$$

where $\underline{e}$ is the experimental noise which corrupts the travel time measurement; $\underline{e}$ is assumed to be uncorrelated with $\underline{\delta T}$ and $\underline{\delta c}$.

The system Eq. (3.1) is highly underdetermined, and thus without additional constraints other than just the data, the system admits infinite number of solutions for $\underline{\delta c}$. In stochastic inverse methods a unique optimal linear estimate of the unknown parameters, $\underline{\delta c}$, can be constructed by incorporating *a priori* knowledge of the parameters in a covariance matrix.

The well known Gauss-Markoff estimator is chosen here because it requires no knowledge of probability densities. This so called *distribution free*

property is the most important feature of the Gauss-Markoff estimator (Liebelt, 1967, pp. 136). The estimate $\underline{\delta c}$ satisfies a *minimum mean square error* criterion

$$\left\langle \left| \underline{\hat{\delta c}} - \underline{\delta c} \right|^2 \right\rangle = \text{minimum.} \tag{3.2}$$

Following Liebelt (1967) and Chiu (1987), the Gauss-Markoff estimate is given by

$$\underline{\hat{\delta c}} = \mathbf{C}_{\underline{\varepsilon}} \mathbf{A}^{\mathrm{T}} \mathbf{C}_{\underline{e}}^{-1} \underline{\delta T}, \tag{3.3}$$

where

$$\mathbf{C}_{\underline{\varepsilon}} = \left[\mathbf{C}_{\underline{\delta c}}^{-1} + \mathbf{A}^{\mathrm{T}} \mathbf{C}_{\underline{e}}^{-1} \mathbf{A} \right]^{-1} \tag{3.4}$$

is the covariance matrix of the error $\underline{\varepsilon} = \underline{\hat{\delta c}} - \underline{\delta c}$ in the estimate, and $\mathbf{C}_{\underline{e}}$ and $\mathbf{C}_{\underline{\delta c}}$ are the covariance matrices of noise $\underline{e}$ and the unknown parameters $\underline{\delta c}$, respectively. The construction of the estimate requires finding the inverse of the matrix $\mathbf{C}_{\underline{\delta c}}^{-1} + \mathbf{A}^{\mathrm{T}} \mathbf{C}_{\underline{e}}^{-1} \mathbf{A}$.

The trading of system resolution for stability in the optimal estimate can be revealed by a singular value decomposition of the matrix $\mathbf{C}_{\underline{e}}^{-\frac{1}{2}} \mathbf{A} \mathbf{C}_{\underline{\delta c}}^{\frac{1}{2}}$ such that

$$\left[\mathbf{C}_{\underline{e}}^{-\frac{1}{2}} \mathbf{A} \, \mathbf{C}_{\underline{\delta c}}^{\frac{1}{2}} \right] = \mathbf{U} \, \Lambda \, \mathbf{V}^{\mathrm{T}}, \tag{3.5}$$

where the diagonal elements λ_i of the matrix Λ are the associated singular values, and the columns $\underline{u}_i$ and $\underline{v}_i$ of $\mathbf{U}$ and $\mathbf{V}$ are the left and right singular vectors, respectively.

The matrix, Eq. (3.5), is the operator associated with a nondimensionalized version of the forward model:

$$\mathbf{C}_{\underline{e}}^{-\frac{1}{2}}\underline{\delta T} = \left[\mathbf{C}_{\underline{e}}^{-\frac{1}{2}}\mathbf{A}\,\mathbf{C}_{\underline{\delta c}}^{\frac{1}{2}}\right]\mathbf{C}_{\underline{\delta c}}^{-\frac{1}{2}}\underline{\delta c} + \mathbf{C}_{\underline{e}}^{-\frac{1}{2}}\underline{e}, \tag{3.6}$$

which is transformed from Eq. (3.1). Using Eq. (3.5), Chiu *et al* (1987) have shown that the minimum mean square error estimate can be expressed as

$$\mathbf{C}_{\underline{\delta c}}^{-\frac{1}{2}}\underline{\hat{\delta c}} = \mathbf{V}\left[\left(\mathbf{I}+\Lambda^{2}\right)^{-1}\Lambda\right]\mathbf{U}^{\mathrm{T}}\;\mathbf{C}_{e}^{-\frac{1}{2}}\underline{\delta T} \tag{3.7}$$

or equivalently as

$$\mathbf{C}_{\underline{\delta c}}^{-\frac{1}{2}}\underline{\hat{\delta c}} = \sum_{i=1}^{k}\frac{\lambda_i}{\lambda_i^{2}+1}\left(\underline{u}_i^{\mathrm{T}}\mathbf{C}_{\underline{e}}^{-\frac{1}{2}}\underline{\delta T}\right)\underline{v}_i \tag{3.8}$$

The vectors $\underline{v}_i$ are the base vectors occupying the solution domain such that any solution can be expressed by a weighted sum of these vectors. A singular value λ_i much small than one is associated with a singular vector $\underline{v}_i$ that models a highly unstable and oscillatory function. The linear estimator downweights these oscillatory function to stabilize the estimate.

B. ERROR AND RESOLUTION

In the previous section, we introduced an estimator which solves the inverse problem. In this section, we derive measures which are used to quantify system performance.

1. Error of the Estimate

The error covariance matrix of the estimate was expressed in Eq. (3.4), which can also be equated, using Eq. (3.5), as

$$\mathbf{C}_{\underline{\varepsilon}} = \mathbf{C}_{\underline{\delta c}}^{\frac{1}{2}}\left[\mathbf{I}-\mathbf{V}\Lambda\left(\mathbf{I}+\Lambda^{2}\right)^{-1}\Lambda\,\mathbf{V}^{\mathrm{T}}\right]\mathbf{C}_{\underline{\delta c}}^{\frac{1}{2}}. \tag{3.9}$$

The diagonal terms of this matrix are the mean square errors of the estimate at each box.

The error of the estimate, $\underline{\delta\hat{c}} - \underline{\delta c}$, has two components, bias and random error. The bias, $b = \langle \underline{\delta\hat{c}} \rangle - \underline{\delta c}$, results from an insufficient number of data, and the random error, $\Delta(\underline{\delta\hat{c}}) = \underline{\delta\hat{c}} - \langle \underline{\delta\hat{c}} \rangle$ is caused by the random experimental noise. Since these two components are statistically independent, $C_{\underline{\varepsilon}}$ can be expressed as

$$C_{\underline{\varepsilon}} = \left\langle \mathbf{b}\mathbf{b}^{T} \right\rangle + C_{\Delta(\underline{\delta c})}, \tag{3.10}$$

where

$$C_{\Delta(\underline{\delta\hat{c}})} = C_{\underline{\varepsilon}} \mathbf{A}^{T} C_{\underline{\varepsilon}}^{-1} \mathbf{A}\, C_{\underline{\varepsilon}} \tag{3.11}$$

or equivalently,

$$C_{\Delta(\underline{\delta\hat{c}})} = C_{\underline{\delta c}}^{\frac{1}{2}} \left[\mathbf{V} \left(1+\Lambda^{2} \right)^{-1} \Lambda^{2} \left(\mathbf{I} + \Lambda^{2} \right)^{-1} \mathbf{V}^{T} \right] C_{\underline{\delta c}}^{\frac{1}{2}}. \tag{3.12}$$

An expression for $\langle \mathbf{b}\mathbf{b}^{T} \rangle$ can be obtained by letting the random error covariance $C_{\Delta(\underline{\delta\varepsilon})}$ approaches zero, i.e. by letting all the eigenvalues λ_i approach infinity in Eq. (3.9). The result is

$$\left\langle \mathbf{b}\mathbf{b}^{T} \right\rangle = C_{\underline{\delta c}}^{\frac{1}{2}} \left[\mathbf{I} - \mathbf{V}\mathbf{V}^{T} \right] C_{\underline{\delta c}}^{\frac{1}{2}}. \tag{3.13}$$

2. Resolution

We define a symmetric, n×n matrix

$$\mathbf{R} = \mathbf{V}\Lambda \left(\mathbf{I} + \Lambda^{2} \right)^{-1} \Lambda\, \mathbf{V}^{T}, \tag{3.14}$$

as the resolution matrix. Using the definition of **R**, Eq. (3.9) becomes

$$\mathbf{C}_{\underline{\varepsilon}} = \mathbf{C}_{\underline{\delta c}}^{\frac{1}{2}} \left[\mathbf{I} - \mathbf{R} \right] \mathbf{C}_{\underline{\delta c}}^{\frac{1}{2}} . \tag{3.15}$$

If the resolution matrix is an identity matrix (that is, **R=I**), then the error is zero. On the other hand, if the resolution matrix is not an identity matrix, for example, if it has nonzero diagonal elements then the error is nonzero. This implies that the mean square error is intimately related to system resolution. The *i*th row of the resolution matrix, $\{\underline{r}_i\}^T$, is defined as the resolution kernel of the *i*th box and it describes how much neighboring boxes contribute to the error of the estimate in the *i*th box, or how well the field at the *i*th box can be resolved (Menke, 1984, pp. 61-68). Figure 3-1 illustrates the structure of a typical resolution matrix.

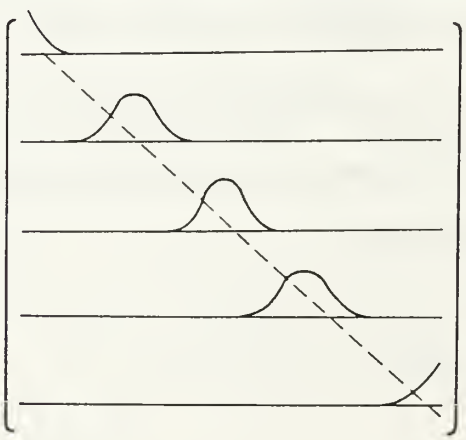

Figure 3-1: Plot of Selected Rows and Columns of The Resolution Matrix R.

If the *i*th resolution kernel has a single spike centered at the diagonal, then the *i*th box is perfectly resolved. If the peak is very broad, the *i*th box is

poorly resolved and has a large error due to the fact that the estimate at the ith box is an average of the neighboring field. In an other word the energy in the estimate is spread to neighboring boxes due to the poor resolving power of the system.

Two measures of the resolution of the estimator have been proposed. One is the so called resolution "spread" (Miller, 1989, pp. 333), which measures the difference between the resolution matrix and an identity matrix via the expression

$$\text{spread} = \sum_{i=1}^{n} \sum_{j=1}^{n} (R_{ij} - I_{ij})^2 , \tag{3.16}$$

The second measure is the so called minimum resolution length (Chiu, 1987), which measures the local resolution at each box location. The resolution length is defined to be the distance at which the resolution energy falls to half of its peak value. To be more precise the minimum resolution length at the ith box is defined as the square root of the second central moment of energy distribution in the ith resolution kernel ($\{\underline{r}_i\}^T$). The minimum resolution lengths in the three spatial directions may be expressed as

$$\mathcal{H}_x(ix,iy,iz) = \sqrt{\sum_{jx}^{nx} \sum_{jy}^{ny} \sum_{jz}^{nz} [(jx - ix)\, dx]^2 \frac{r_i^2(jx,jy,jz)}{E_i}} , \tag{3.17.a}$$

$$\mathcal{H}_y(ix,iy,iz) = \sqrt{\sum_{jx}^{nx} \sum_{jy}^{ny} \sum_{jz}^{nz} [(jy - iy)\, dy]^2 \frac{r_i^2(jx,jy,jz)}{E_i}} , \tag{3.17.b}$$

and

$$\mathcal{V}(ix,iy,iz) = \sqrt{\sum_{jx}^{nx}\sum_{jy}^{ny}\sum_{jz}^{nz} [\,(jz - iz)\,dz\,]^2 \frac{r_i^2(jx,jy,iz)}{E_i}}\,, \tag{3.17.c}$$

where E_i is the total energy of the ith resolution kernel $\underline{r}_i^T$.

$$E_i = \sum_{jx}^{nx}\sum_{jy}^{ny}\sum_{jz}^{nz} r_i^2(jx,jy,jz)\,. \tag{3.17.d}$$

In Eq. (3.17.a-b) $\mathcal{H}_x$ and $\mathcal{H}_y$ are the minimum horizontal resolution lengths in the x and y directions, respectively, while $\mathcal{V}$ is the minimum vertical resolution length. Physically, the minimum resolution lengths determine the minimum eddy size that can be resolved adequately by the monitoring system. Note that we have expanded the row index i and column index j into three dimensional box indices, (ix, iy, iz) and (jx, jy, jz), in Eqs. (3.17.a-d). The expansion was done according to the following equations.

$$i = (ix\text{-}1)\times ny\times nz + (iy\text{-}1)\times nz + iz = 1, 2, ...n, \tag{3.18.a}$$

$$j = (jx\text{-}1)\times ny\times nz + (jy\text{-}1)\times nz + jz = 1, 2, ...n \tag{3.18.b}$$

with

$$n = nx\times ny\times nz, \tag{3.18.c}$$

where ix, jx = 1, 2, ...nx, is box indices in the x direction; iy, jy = 1, 2, ...ny, is box indices in the y direction; iz, jz = 1, 2, ...nz, is box indices in the z direction. With nx = 10, ny = 10, and nz = 5, the total number of boxes is n = 500.

From the above discussion in this chapter, It has been found that the RMS error and resolution length do not depend on the experimental data $\underline{\delta T}$, but only on the sound speed perturbation covariance matrix $C_{\underline{\delta c}}$, travel time error

covariance matrix $\mathbf{C}_{\underline{e}}$, and the transfer function A (which depends on the array geometry and the number of rays).

IV. RESULTS OF SENSITIVITY STUDY

In the last chapter, we outlined two ways to evaluate the performance of the Greenland Sea tomography array by examining the statistics of the error in the estimate and the resolution of the system. As mentioned the RMS error of the estimate and the system resolution measures depend on the covariance matrix of sound speed perturbation $\mathbf{C}_{\underline{\delta c}}$, the covariance matrix of noise $\mathbf{C}_{\underline{e}}$, the array geometry, the number of eigenrays but not the data $\underline{\delta T}$. Therefore, even without using actual or synthetic measurements, the performance of the array and ray path geometry can be evaluated given the covariances. By varying the ocean correlation length (which determines $\mathbf{C}_{\underline{\delta c}}$), the rms value of noise (which determines $\mathbf{C}_{\underline{e}}$), and the array geometry (which determines $\mathbf{A}$), we have examined the changes in system performance as these ocean and acoustic parameter vary. The results are discussed in Section IV-B.

By incorporating statistical information concerning the covariance of the field, the indeterminacy of the unknown field, $\underline{\delta c}$, is eliminated. Since the covariance matrix $\mathbf{C}_{\underline{\delta c}}$ is the *a priori* information that we supply to the estimator, we are particularly interested in determining the sensitivity of the estimate to the uncertainties in the correlation lengths of the sound speed perturbation field. This sensitivity study was accomplished through inversions of synthetic data generated in the computer. The results are discussed in Section IV-C.

In the following section, we first discuss the method we use to simulate sound speed perturbation fields and travel time data in the computer.

A. COMPUTER SIMULATION OF MESOSCALE SOUND SPEED FIELDS AND TRAVEL TIME DATA

The temperature, sigma-t, and sound speed profiles obtain by a CTD (Conductivity, Temperature, and Density) cast in the Greenland Sea (Worcester and Howe, 1989) is shown in Figure 4-1. We have superimposed on this data a linear profile (dash line) which we have chosen as the reference sound speed profile. In the simulation work, we take that the perturbations of sound speed occur only in the water column shallower than 1,000 m. This is not a bad assumption as indicated by CTD profile obtained by Worcester and Howe. For simplicity, we also neglect ocean currents in our analysis and work with forward transmission paths only.

In the reconstruction of the sound speed perturbation field, the correlation covariance function of the field (or its discretized version, i.e., the covariance matrix $\mathbf{C}_{\underline{\delta c}}$.) needs to be specified. We assume that the sound speed perturbation field is homogeneous and has a gaussian shape so that we can specify the correlation between the field at two different points in an analytical form as

$$\mathrm{Cov}(\Delta x,\Delta y,\Delta z) = \sigma^2_{\underline{\delta c}} e^{-\left[\left(\frac{\Delta x}{L_x}\right)^2 + \left(\frac{\Delta y}{L_y}\right)^2 + \left(\frac{\Delta z}{L_z}\right)^2\right]} \tag{3.8}$$

where Δx is the horizontal separation between the two points in the x-direction, Δy is the horizontal separation in the y-direction, and Δz is the vertical separation. The correlation length, Lx, Ly, and Lz, determine the correlation scale of the field. TABLE 4-1 summarizes the various sets of correlation lengths (Lx, Ly, and Lz) that we used to simulate the sound speed perturbation fields of different scales. For all the simulated fields, we use $\sigma_{\underline{\delta c}} = 5$ m/s.

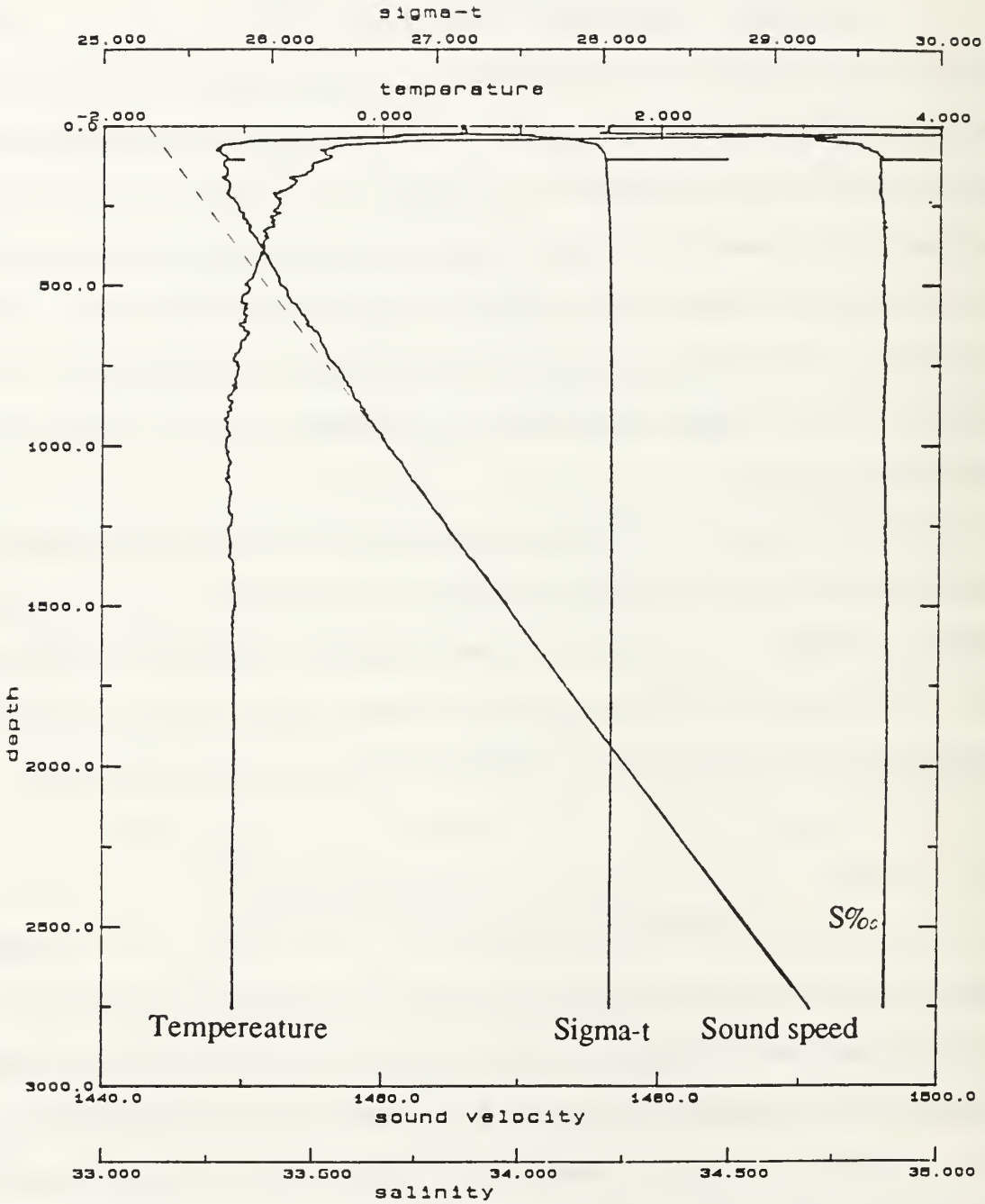

Figure 4-1: The CTD Data of Mooring #1 From the Deployment Cruise (Worcester and Howe, 1989).

TABLE 4-1 : THE SIMULATED OCEAN VOLUME.

Ocean volume	L_x (km)	L_y (km)	L_z (km)
Eddy204	20	20	0.4
Eddy304	30	30	0.4
Eddy404	40	40	0.4

In order to perform simulation inversions in the computer, we need to generate a set of travel time data for input to the estimator. A normal random deviate generator is used to generate realizations of a random process having a specified covariance. This random deviate generator is used to simulate the sound speed perturbation and noise fields. The simulated fields are then combined using the model (given by Eq. (2.9)) to give the simulated travel time data. A block diagram of the process is shown in Figure 4-2.

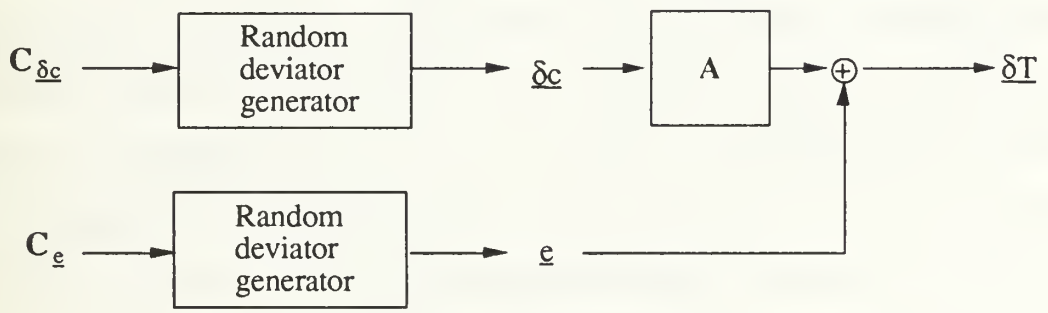

Figure 4-2 : The Block Diagram of Travel Time Generation.

The generated travel time data with additive random noise are the input to the estimator. An estimate of the sound speed field, $\underline{\delta \hat{c}}$ is the inverse result, which depend on the matrices $C_{\underline{\delta c}}$, $C_{\underline{e}}$ and **A** in addition to the data themselves. The sensitivity of the system can thus be evaluated for changes in correlation

length of the sound speed perturbation field, changes in noise level, changes in array geometry due to mooring failure, etc. To simulate noise-free measurements, we use a very small noise level with an rms value of $\sigma_{\underline{\epsilon}} = 0.1$ ms.

The *optimal* estimate is obtained when the correlation length used for inversion is exactly the same as that actually present in the ocean volume (that is, when the *a priori* covariance $\mathbf{C}_{\underline{\delta c}}$ is correct). In fact, because the *a priori* covariance is never exactly known, optimal estimates are generally hard to obtain. The quality of *suboptimal* estimates can be evaluated by studying the effect of correlation length uncertainties ΔL_x, ΔL_y, and ΔL_z on the performance of the estimator.

B. SYSTEM PERFORMANCE

1. RMS Error Analysis

The local RMS error as a function of box index *j* in the estimate (that is, the RMS error at the *j*th box) can be obtained by evaluating the square root of the *j*th element along the diagonal of the estimate error covariance matrix $\mathbf{C}_{\underline{\epsilon}}$. This local RMS error gives a picture of how the errors are distributed spatially. The square root of the spatial average of the mean square errors at each of the boxes, σ_E, was calculated to get an idea of how much the local error varies over the whole ocean volume being studied.

Figure 4-3 shows the contour plots of the local RMS estimate error for one set of system parameters in each of the five vertical layers. The RMS error for this case is approximate from 1 m/s to 2.5 m/s (or 20% to 50% compared to the 5 m/s signal level) and shows gradual dependence on horizontal or vertical position inside the perimeter of the array. The error outside the array's perimeter increases rapidly as distance from the array increases. Obviously, we

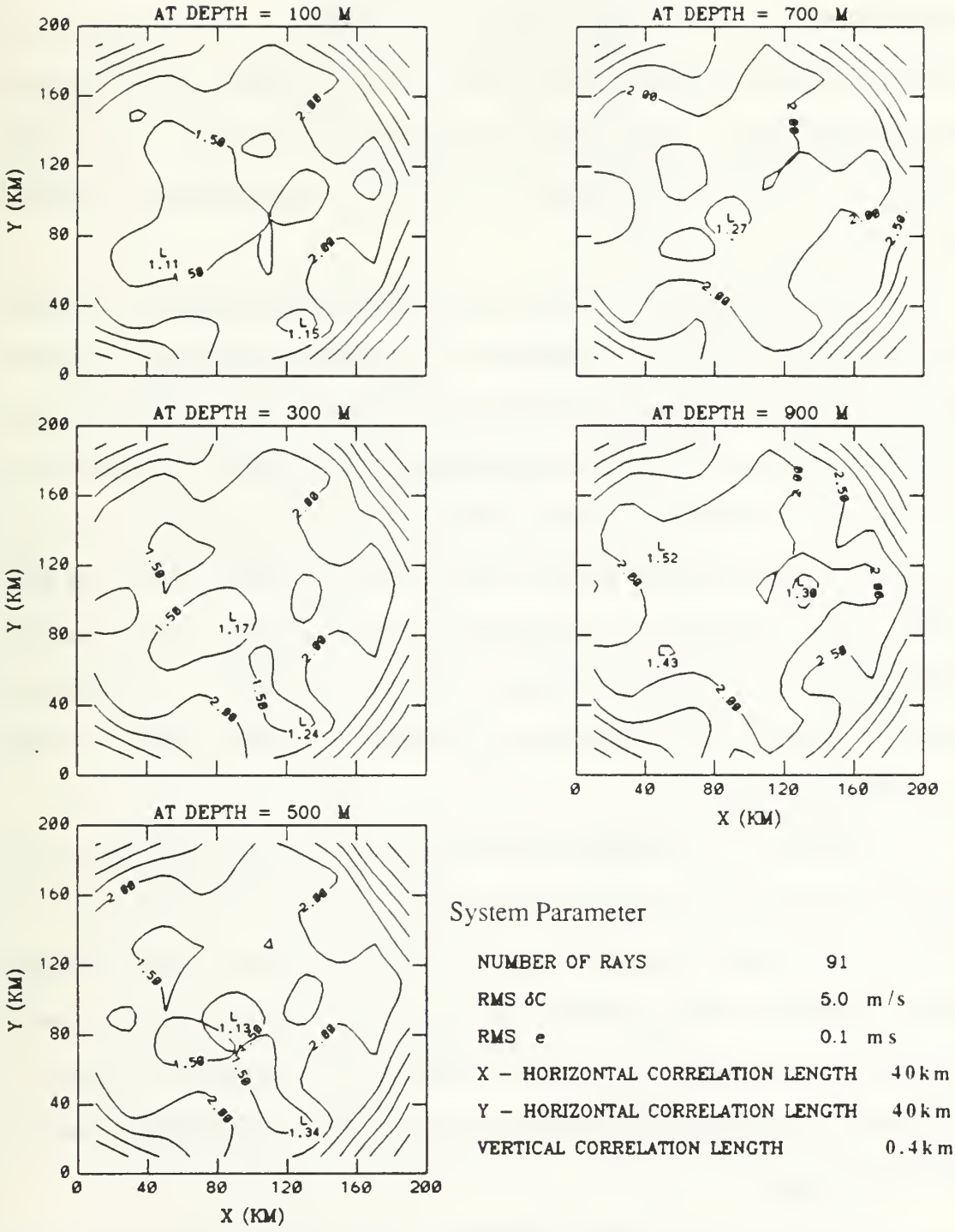

System Parameter

NUMBER OF RAYS	91
RMS δC	5.0 m/s
RMS e	0.1 ms
X – HORIZONTAL CORRELATION LENGTH	40km
Y – HORIZONTAL CORRELATION LENGTH	40km
VERTICAL CORRELATION LENGTH	0.4km

Figure 4-3: RMS Error (m/s) at Each Layer. The contour level is 0.5 m/s.

cannot obtain accurate estimate of the sound speed perturbations for points outside the array. There is little difference between the RMS errors in the individual layers because each vertical layer are well sampled by the eigenrays whose turning points occupy every layer. Because of the rather weak vertical dependence, in the following discussion we present only the analysis for the first layer.

The local RMS error maps for the first layer for different horizontal correlation lengths are shown in Figure 4-4. The system parameters are identical to those of Figure 4-3, except that the horizontal correlation length is varied from 20 km to 60 km in a 10 km step. We see that a wider covariance matrix (*i.e.*, a longer correlation length) results in a lower estimate error. This observation is not surprising, since a longer correlation length means that there is more gradual variation in sound speed perturbation with position, and that neighboring boxes are more correlated. An increased correlation reduces the number of degrees of freedom in the solution, and thus giving a better determined solution.

In Figure 4-5, the maps are generated using the system parameters identical to those used to generate Figure 4-3, except that the vertical correlation length is varied from 0.2 km to 0.6 km in a 0.1 km step at a fixed horizontal correlation length of 40 km. There is less change in RMS error over the entire range of correlation lengths for this case than for the case shown in Figure 4-4. This is because the eigenrays sample the vertical layer more adequately than the horizontal sections.

The effect of an increased (or decreased) noise level on the estimate are shown in Figure 4-6. A higher noise level results only in a slightly higher RMS

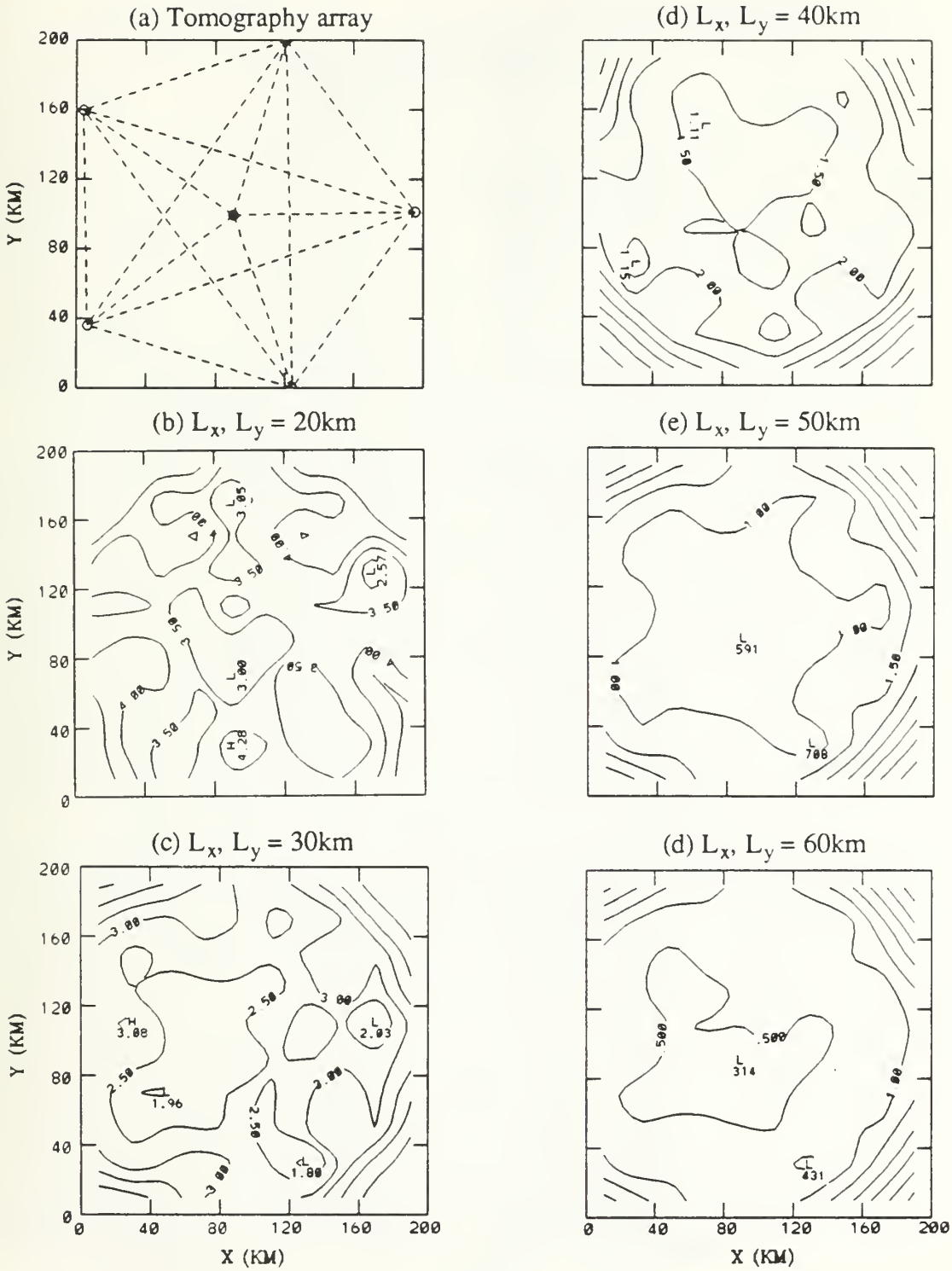

Figure 4-4: Estimate RMS Error (m/s). The contour level is 0.5 m/s. The vertical correlation length L_z is fixed at 0.4 km.

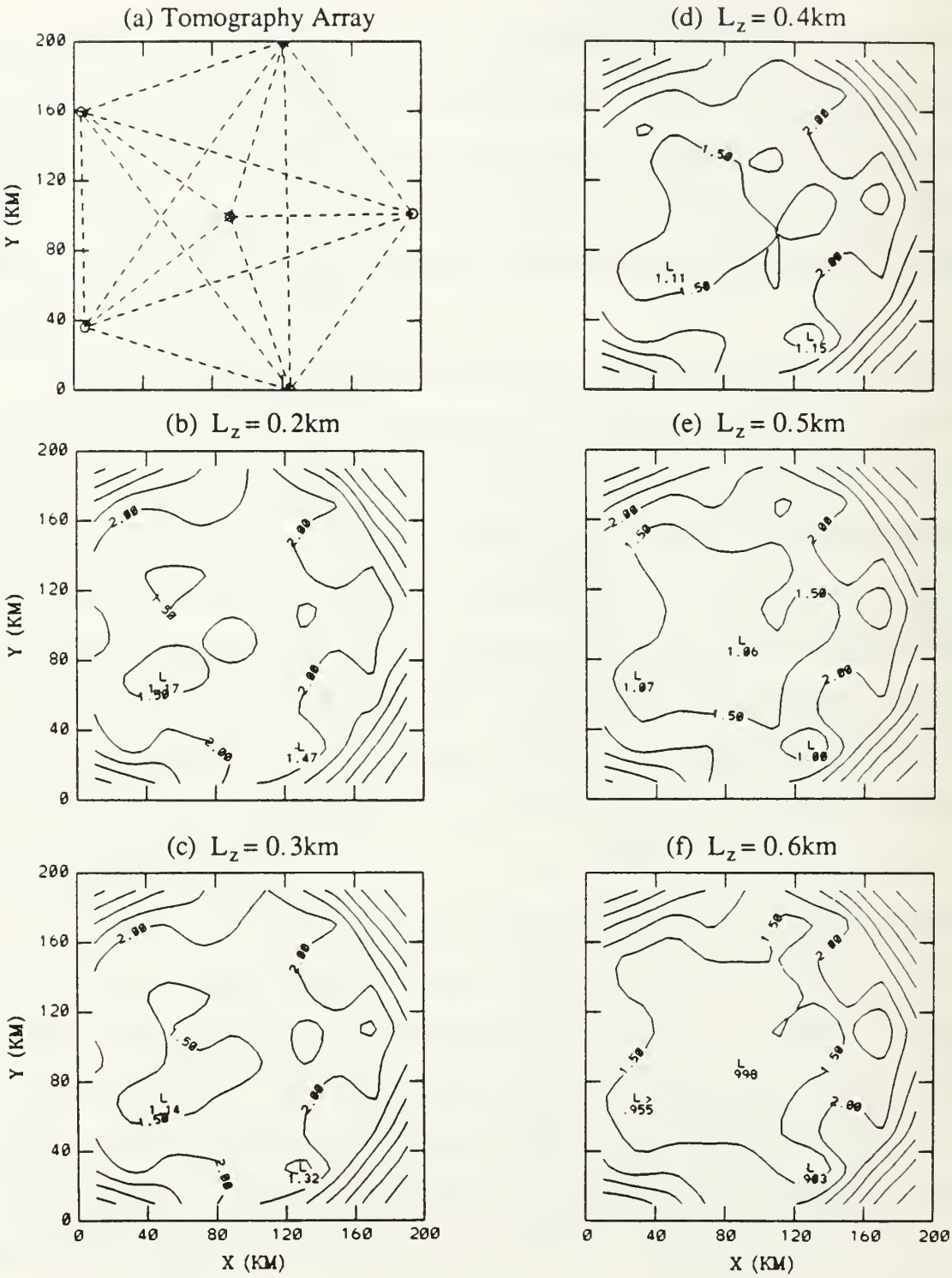

Figure 4-5: Estimate RMS Error (m/s). The contour level is 0.5 m/s. The horizontal correlation length L_x and L_y is fixed at 40 km.

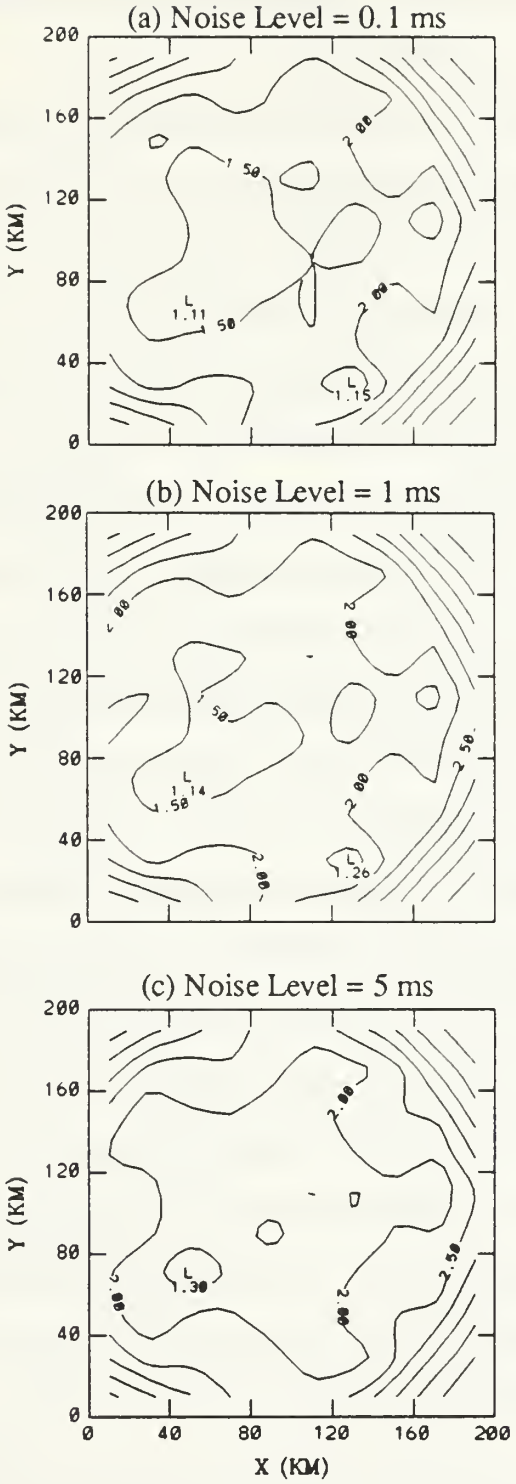

Figure 4-6: Estimate RMS Error at Different Noise Levels. The contour level is 0.5 m/s.

error. The estimate is thus not as strongly affected by changes in noise as it is by changes in the ocean correlation length.

Figure 4-7 shows the effect of array element failure on the RMS error (the array configuration is superimposed on the contour plots to give an idea of how the estimate depends on the array configuration). Within the perimeter of the remaining "good" elements, the RMS errors are only about 25% (0.5 m/s) higher than those given by the full array (2.0 m/s). However, the errors outside the area covered by the good elements increase rapidly to 100%. The failure of array elements has a very pronounced effect on the estimate, especially when two or more elements fail. The system essentially loses its ability to give accurate estimates in areas that do not have rays passing through them.

A single measure of RMS error can be evaluated by calculating a spatial "average" of the individual local errors. We use σ_E for such a global measure and it is computed by assuming the individual mean-square errors at all the box locations and then taking the square root of that sum. Figures 4-8 and 4-9 show σ_E as a function of the ocean horizontal and vertical correlation lengths, respectively, for various array geometries and noise levels. In all cases, σ_E was found to decrease with increasing L_x and L_y (see Figure 4-8). However, σ_E is not as sensitive to changes in L_z as it is to changes in L_x and L_y (see Figure 4-9). This is due to the fact that the vertical structure is sampled adequately whereas the horizontal structure is not. In view of this, in the following discussion, we will only discuss the sensitivity of the results of our resolution analysis with the vertical correlation length fixed at 0.4 km.

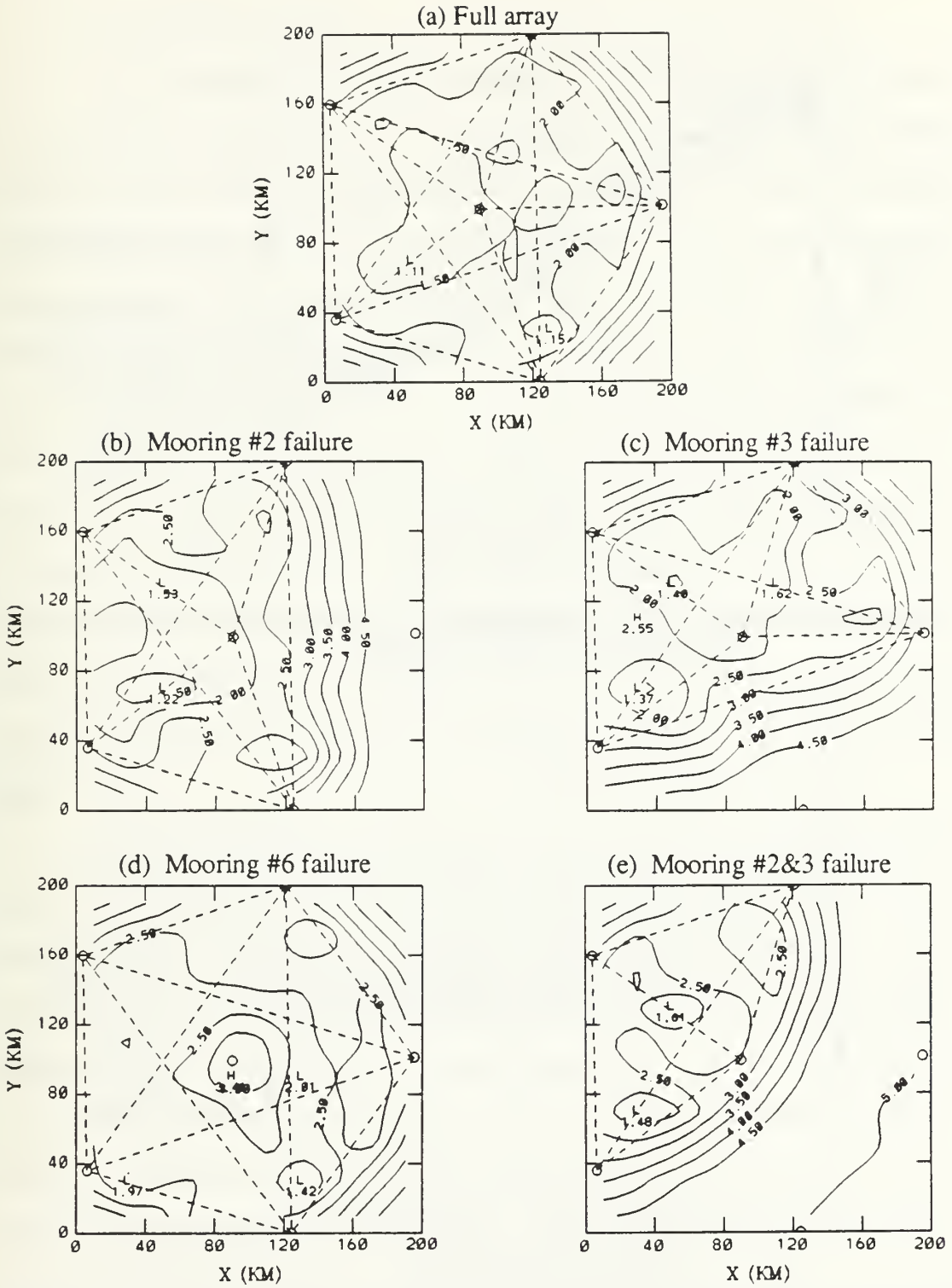

Figure 4-7: Estimate RMS Error (m/s) in Mooring Failure Cases. The contour level is 0.5 m/s. $L_x = L_y = 40$ km, and $L_z = 0.4$ km.

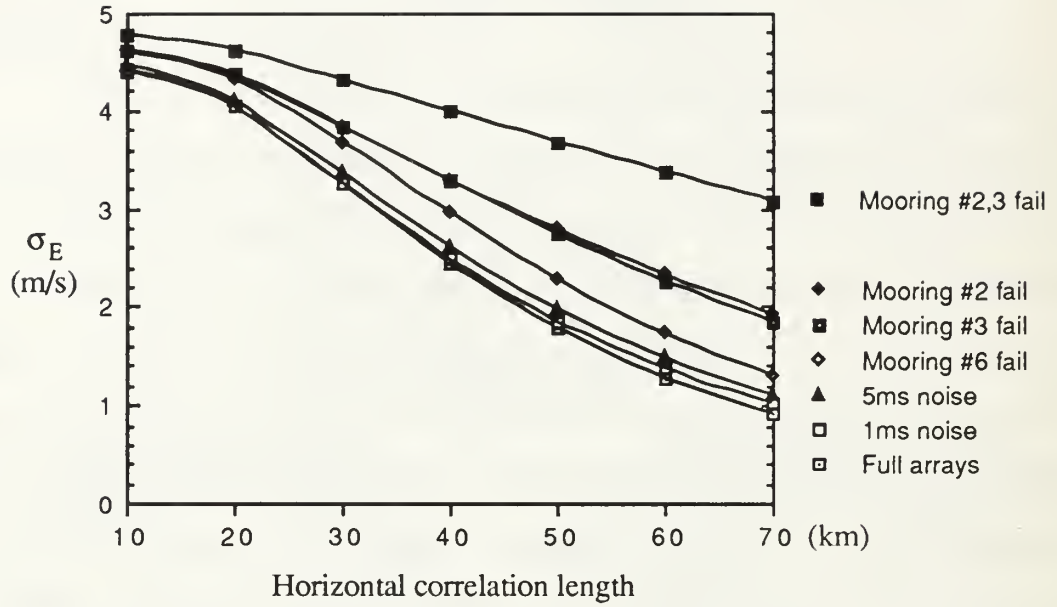

Figure 4-8: Square Root of Spatial Average Mean Square Error vs. Horizontal Correlation Length.

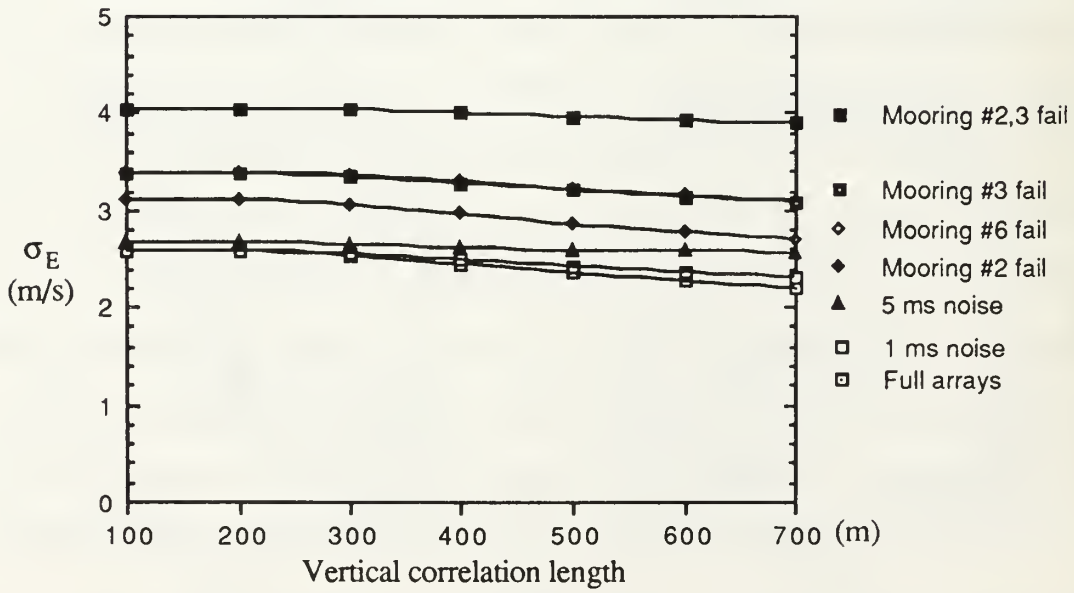

Figure 4-9: Square Root of Spatial Average Mean Square Error vs. Vertical Correlation Length.

2. Resolution Analysis

Two measures of system resolution were defined in the last chapter. One measure is the minimum resolution length, which gives the local resolution at each box. The minimum resolution length is essentially the size of the smallest ocean feature which can be resolved by the array. A large minimum resolution length indicates a poor resolving power. Figure 4-10 shows the minimum resolution length $\mathcal{H}_x$ in the x direction as a function of L_x and L_y. We see that for L_x and L_y greater than 30 km, $\mathcal{H}_x$ is relatively constant over the interior of the array and in most of the region of interest. On the other hand, if L_x and L_y are less than or equal to 30 km, $\mathcal{H}_x$ varies heavily on both x and y and becomes very large in regions containing no y-oriented ray paths. The behavior of $\mathcal{H}_y$, the minimum resolution length in the y direction, is analogous to the behavior of $\mathcal{H}_x$ and is shown in Figure 4-11. In general, the average minimum resolution length is approximately 30 km inside the monitored region as shown in Figure 4-10 and Figure 4-11.

Figure 4-12 shows the behavior of $\mathcal{H}_x$ and $\mathcal{H}_y$ as noise level change while the horizontal and vertical correlation lengths are fixed at 40 km and 0.4 km, respectively. We see that varying the noise level has little effect on $\mathcal{H}_x$ and $\mathcal{H}_y$. Figure 4-13 shows how the failure of various array elements affects $\mathcal{H}_x$. A diagram of the array configuration is superimposed on each plot in Figure 4-13 to show the connection between array geometry and $\mathcal{H}_x$. Despite the element failures, $\mathcal{H}_x$ remains relatively constant inside the area covered by the remaining array elements, but it increases rapidly as we move outward from the perimeter. Although there is some resolving power outside the array perimeter, it is highly inadequate.

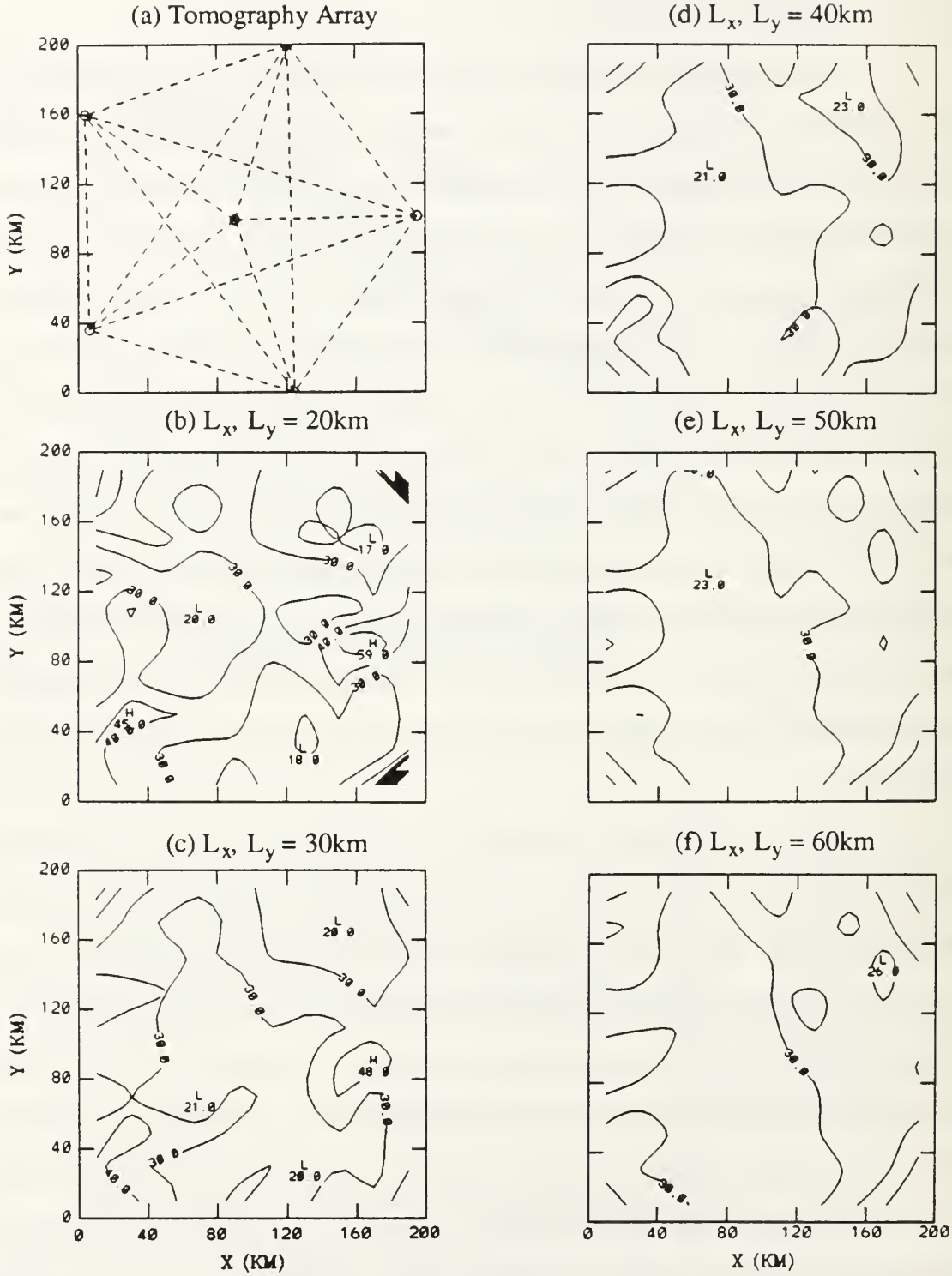

Figure 4-10: Horizontal Minimum Resolution Length $\mathcal{H}_x$. The contour level is 10 km. L_z is fixed at 0.4 km.

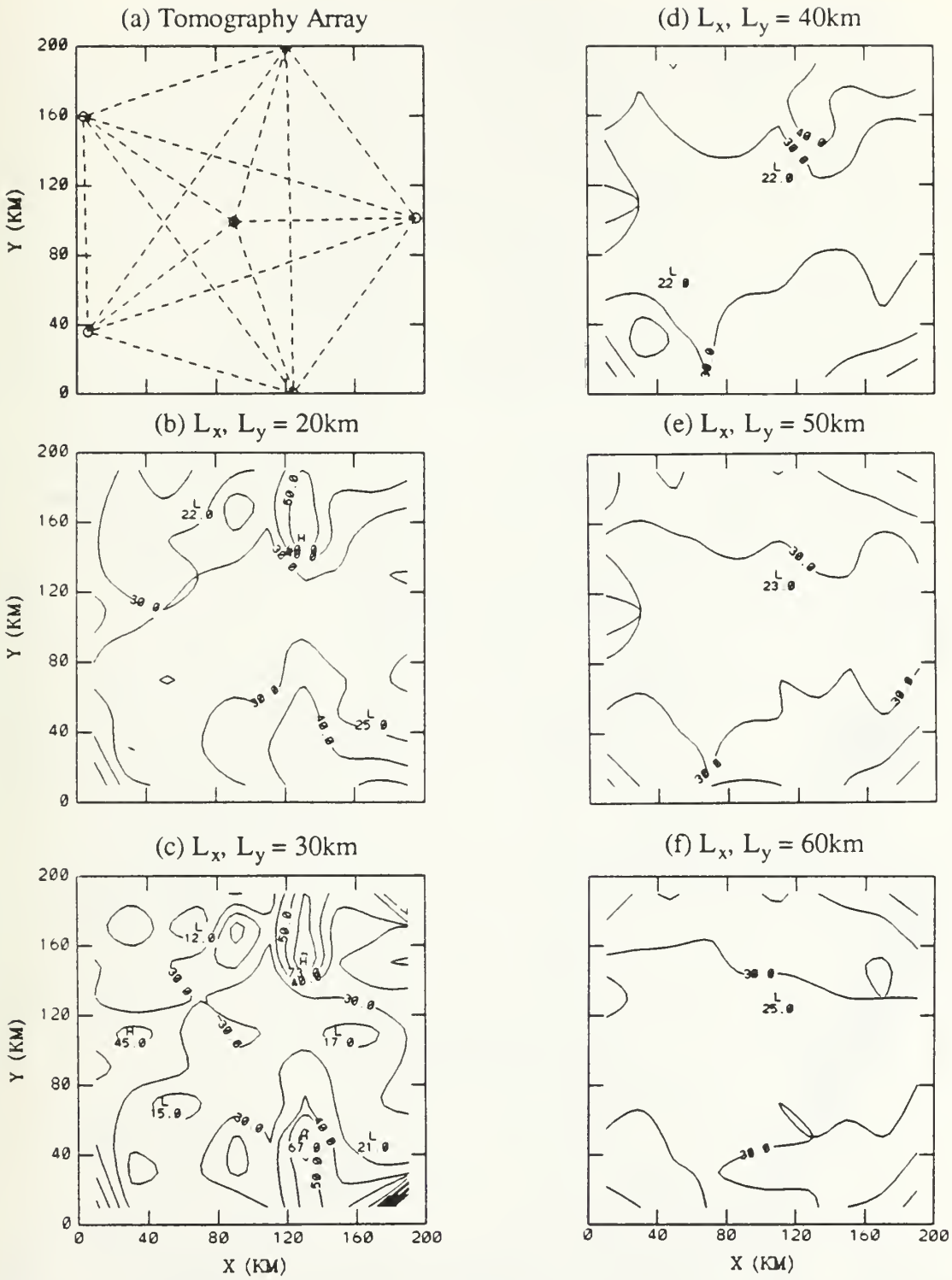

Figure 4-11: Horizontal Minimum Resolution Length $\mathcal{H}_y$. The contour level is 10 km. L_z is fixed at 0.4 km.

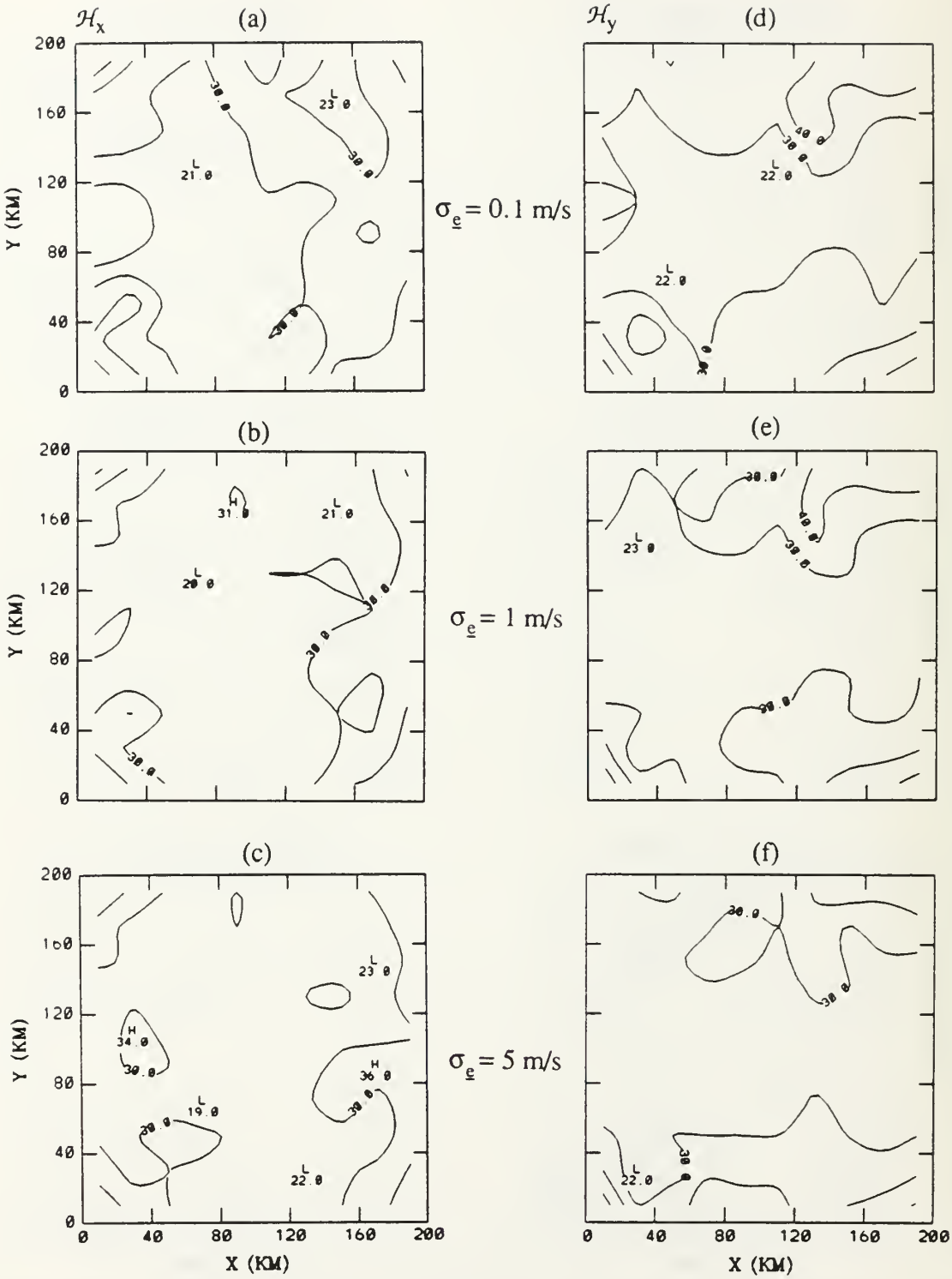

Figure 4-12: Horizontal Minimum Resolution Lengths at different Noise levels. The contour level is 10 km. L_x = L_y = 40 km, and L_z = 0.4 km.

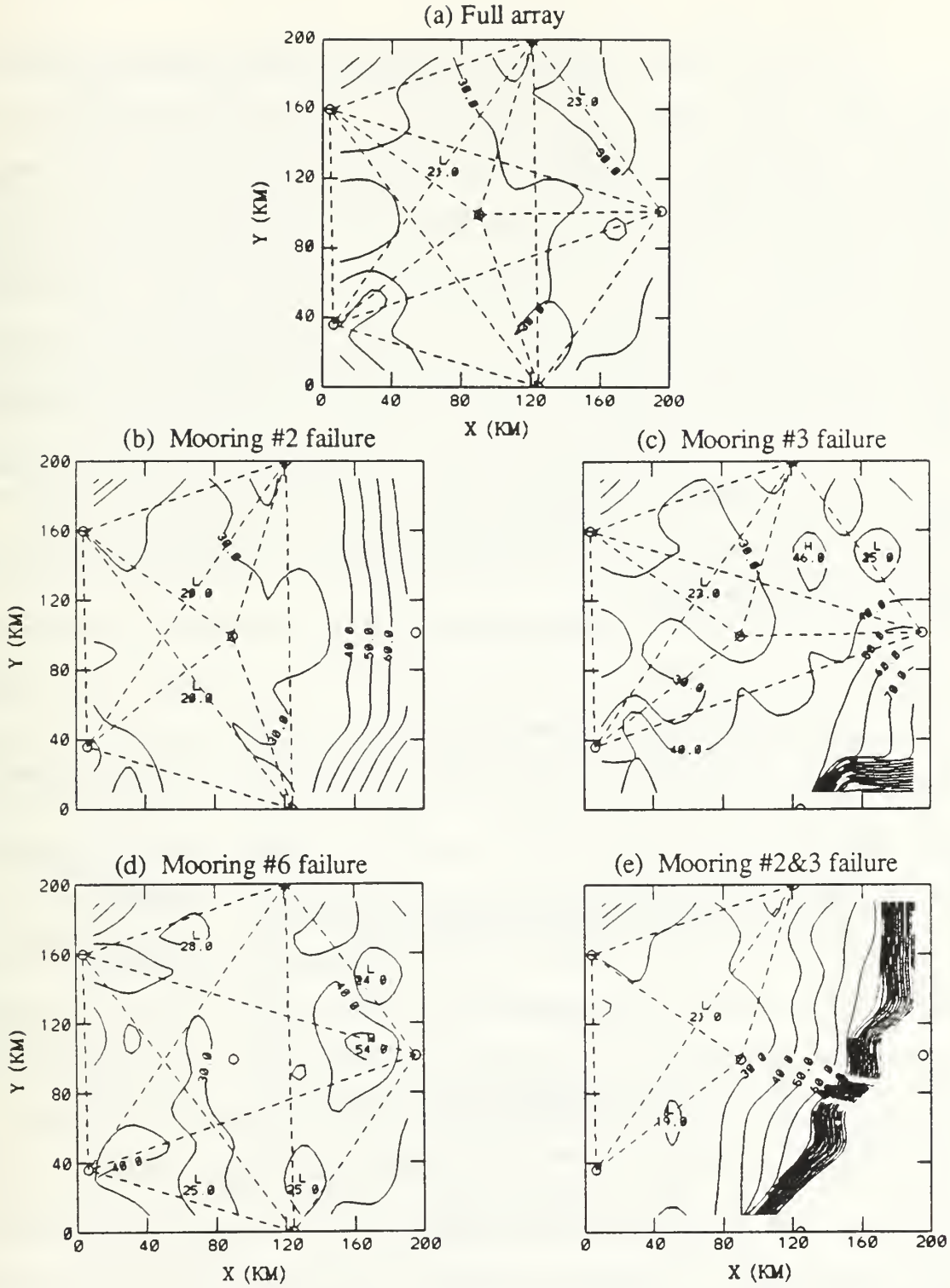

Figure 4-13: Horizontal Minimum Resolution Lengths in various Mooring Failure cases. The contour level is 10 km. $L_x = L_y = 40$ km, and $L_z = 0.4$ km.

The second measure of system resolution is the resolution spread (Eq. 3.16), which is the square of the Frobenius norm of the difference between the resolution matrix and the identity matrix. The resolution spread is thus a single scalar quantity which describes the resolution of an estimator over an entire region. Figure 4-14 shows resolution spread as a function of horizontal correlation length for each of several noise levels and array geometries. We see that the resolution spread does not significantly depend on changes in correlation length, except when noise level is increased. That is, system resolution is a lot more sensitive to changes in correlation length when the system is not noise free. Generally, the resolution spread depends most strongly on the array geometry at any fixed correlation length.

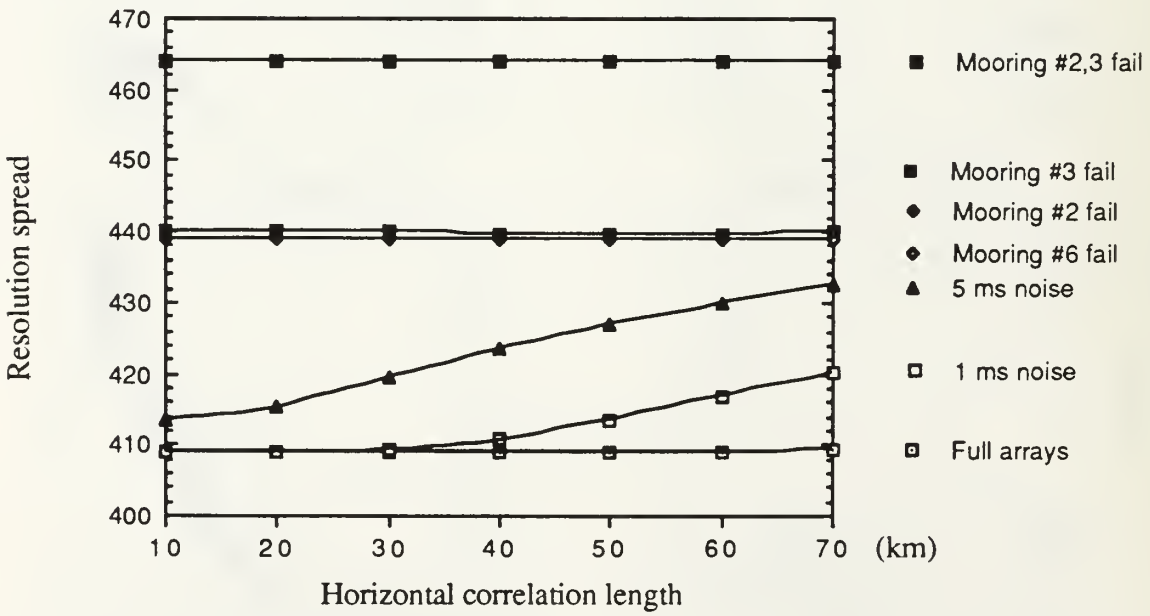

Figure 4-14: Resolution Spread vs. Horizontal Correlation Length.

C. SENSITIVITY OF INVERSE SOLUTION

Synthetic travel time perturbation data $\underline{\delta T}$ (refer to Figure 4-2 for the generation of $\underline{\delta T}$) were used to reconstruct the sound speed perturbation fields $\underline{\delta c}$ simulated in the computer. The sensitivity of the estimate to uncertainty in the correlation length specified for inversion is examined in this section by comparing the suboptimal estimates to the optimal estimates. The optimal estimates are those derived using an exact covariance of the field whereas the suboptimal ones are consequences of inexact covariances.

Figure 4-15 shows the simulated field Eddy404 (refer to TABLE 4-1 for the simulation parameters), its optimal estimate, the associated RMS error as well as the difference between the estimate and the simulated field. The estimate error $\underline{\delta c}-\underline{\delta \hat{c}}$ is low (from 0 to ±2 m/s, which is from 0% to 40% compared to a signal level of 5 m/s) over most of the area inside the array. The error is larger in the left edge and corners. Figures 4-16 compares the estimate errors of some suboptimal estimates generated using correlation lengths differ from the true one. The difference between the assumed horizontal correlation lengths for inversion and the true lengths are denoted by ΔL_x and ΔL_y in the figure. Obviously, the effect of a positive correlation length uncertainty seems less harmful than that of a negative one when the actual correlation length is 40 km.

Figure 4-17 shows the effect of uncertainty in the noise level (i.e., in the noise covariance matrix $C_{\underline{e}}$) on the estimate. The maps on the left are the estimates of the Eddy404 field with various noise level uncertainties $\Delta\sigma_{\underline{e}}$. On the right the associated errors are displayed. Generally, a higher noise level uncertainty gives a higher estimate error, although the differences in the errors are quite minimal.

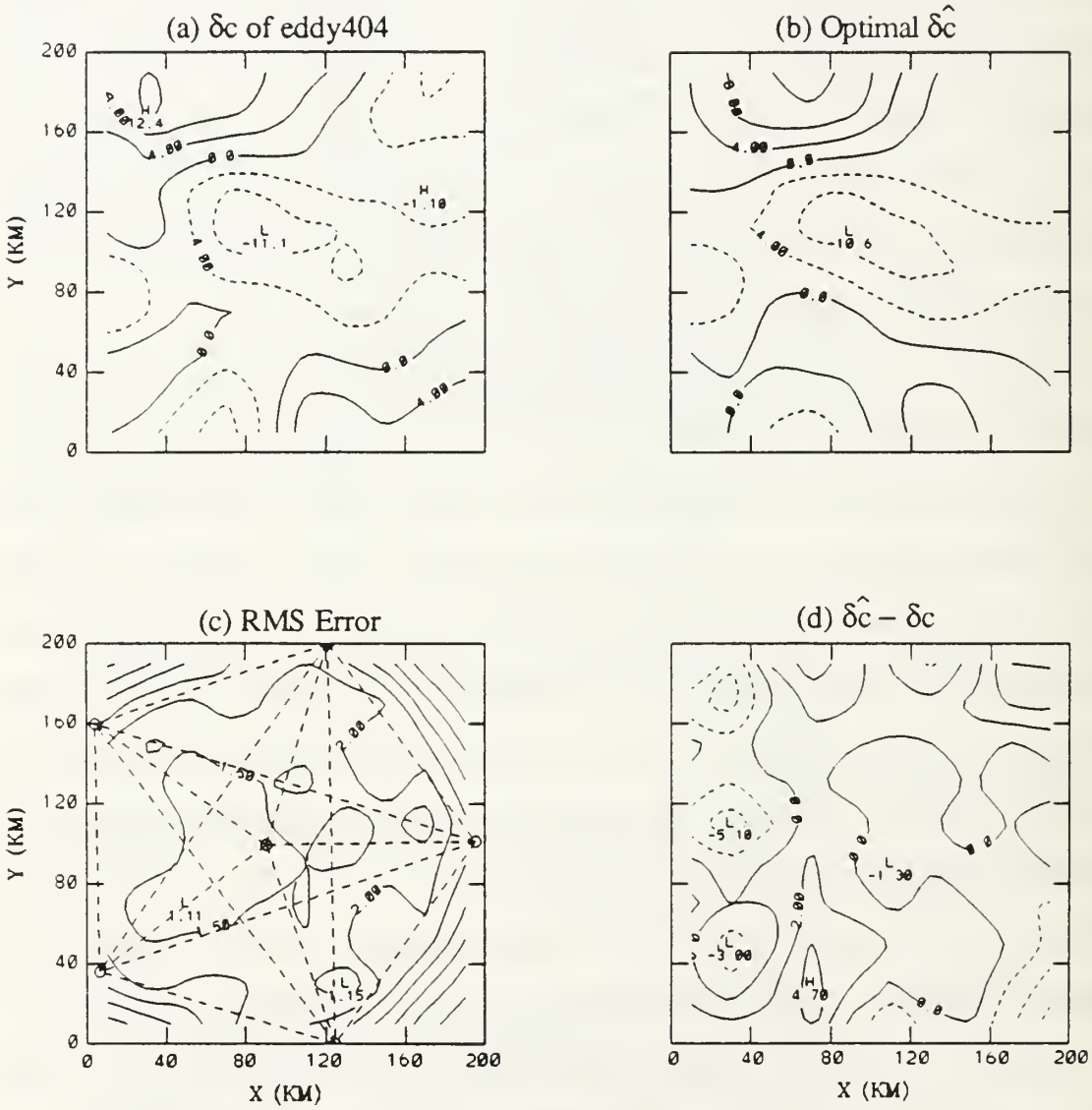

Figure 4-15: A simulated field, its optimal estimate, estimate RMS error, and difference between the optimal estimate and the simulated field. Units are in m/s. $L_x = L_y = 40$ km, $L_z = 0.4$ km, and $\Delta L_x = \Delta L_y = \Delta L_z = 0$.

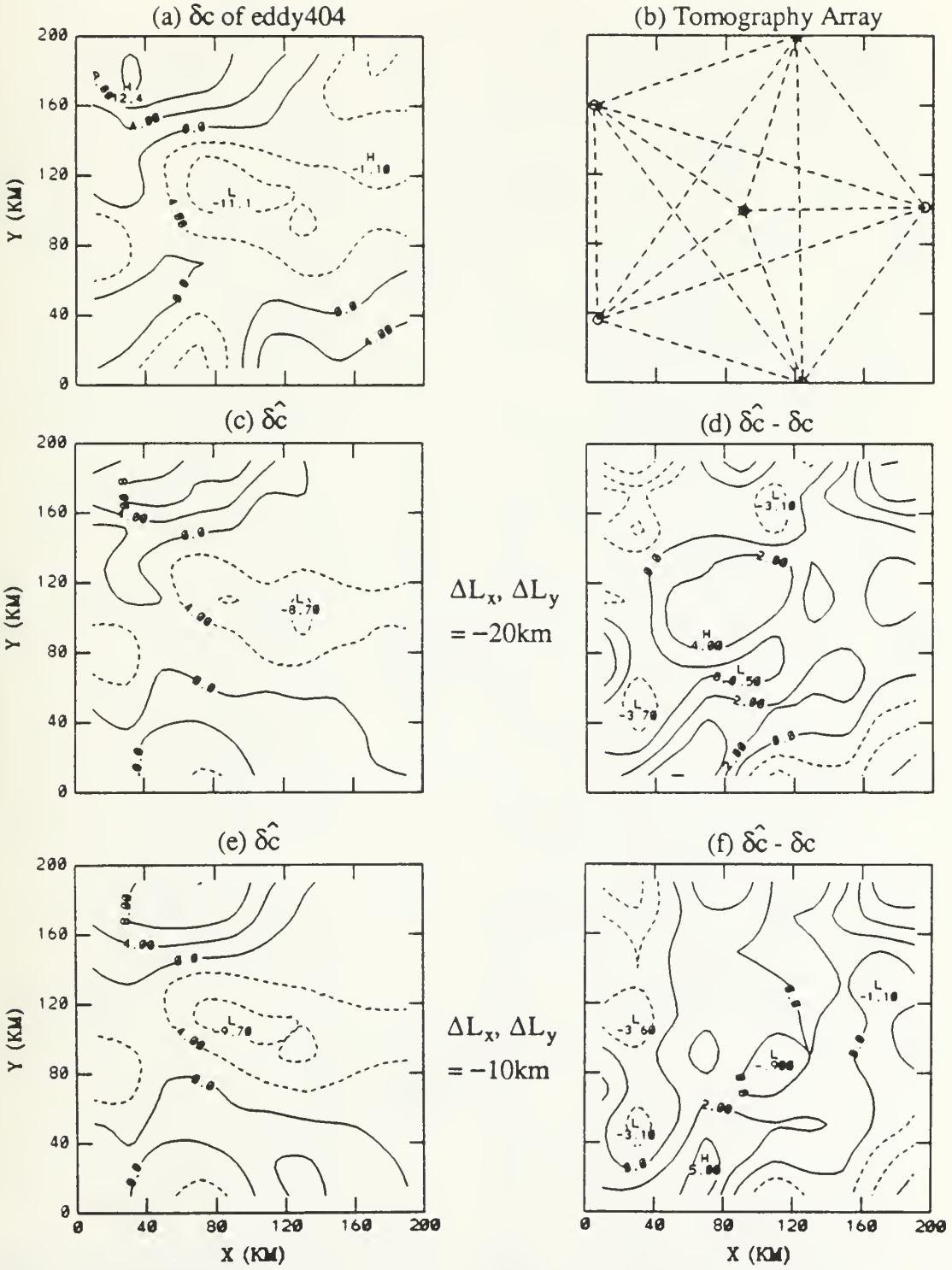

Figure 4-16: Simulated Eddy404 field, suboptimal estimates, and the corresponding true error fields. The contour level is 4 m/s and 2 m/s for $\underline{\delta c}$ and $\underline{\delta \hat{c}} - \underline{\delta c}$, respectively. $L_x = L_y = 40$ km, and $L_z = 0.4$ km.

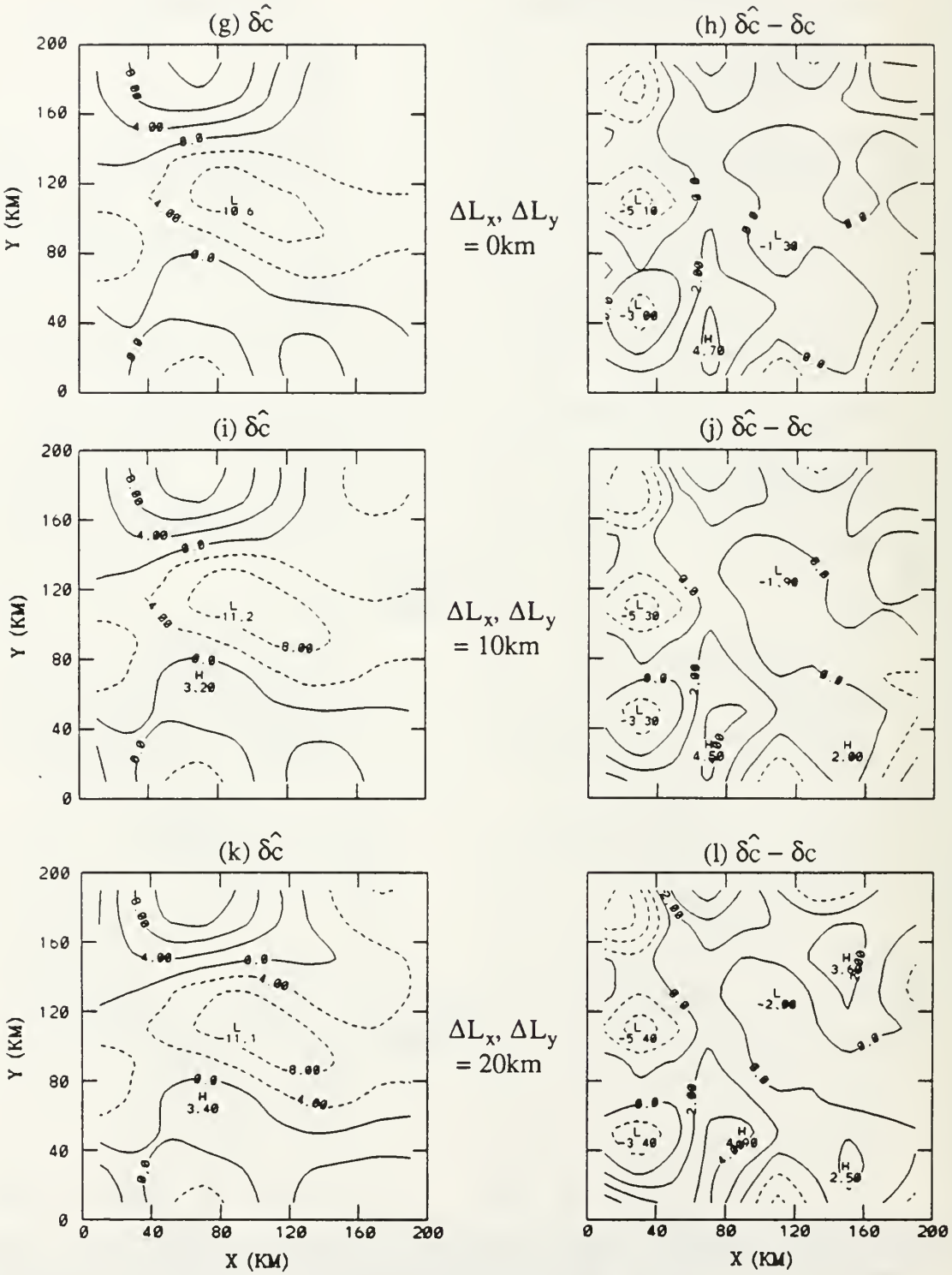

Figure 4-16: (Continued from last page).

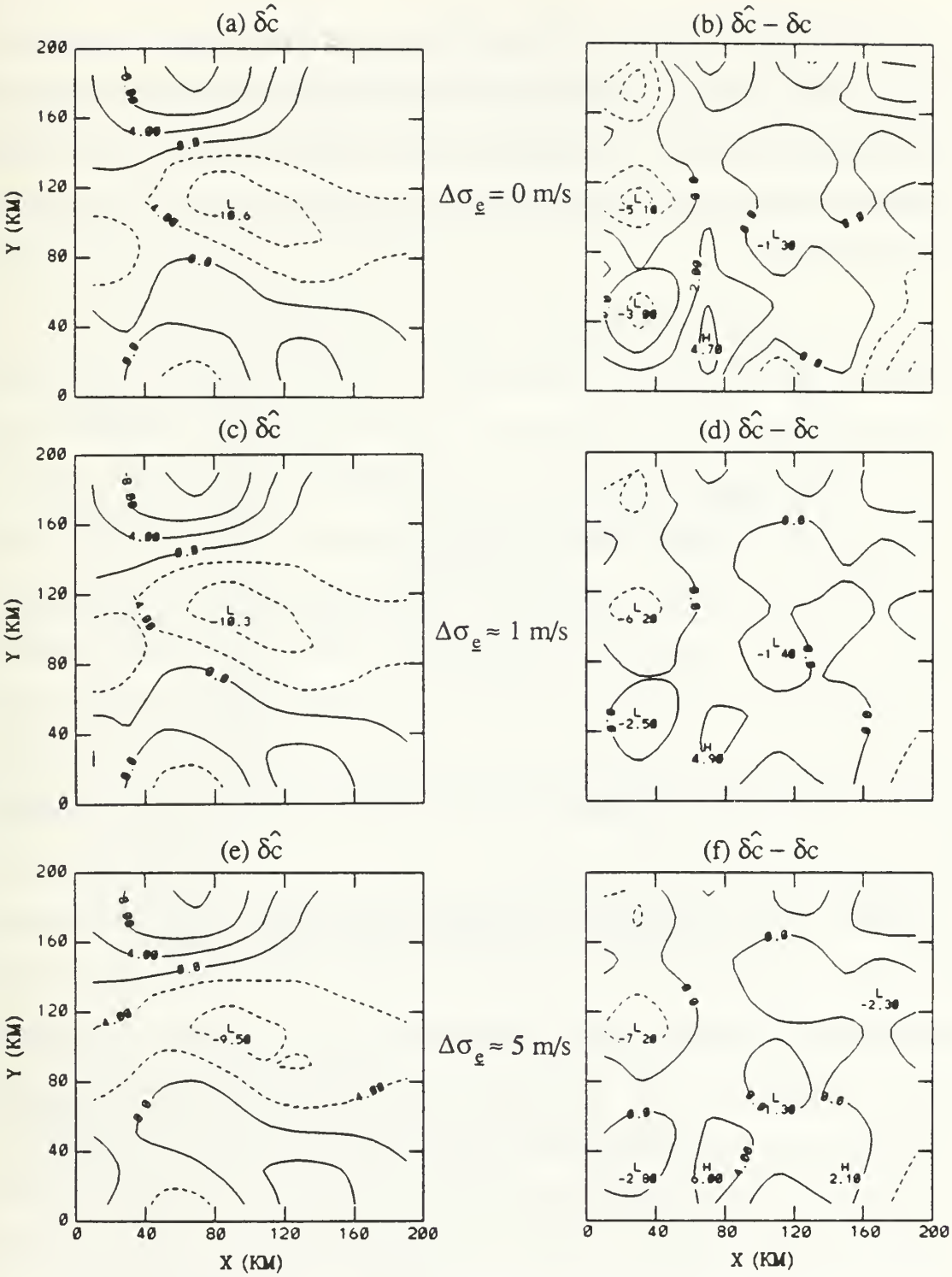

Figure 4-17: Estimation (m/s) with Noise Level Uncertainty. The contour level is 4 m/s and 2 m/s for $\underline{\delta c}$ and $\underline{\delta\hat{c}} - \underline{\delta c}$, respectively. $L_x = L_y = 40$ km, and $L_z = 0.4$ km.

To gain insight into the global performance of the estimator, we calculated σ_ξ, the square root of the spatial average of the local squared errors. Figure 4-18 shows σ_ξ as a function of horizontal correlation uncertainty for each of the three simulated ocean volumes having horizontal correlation length of 20, 30 and 40 km, respectively.

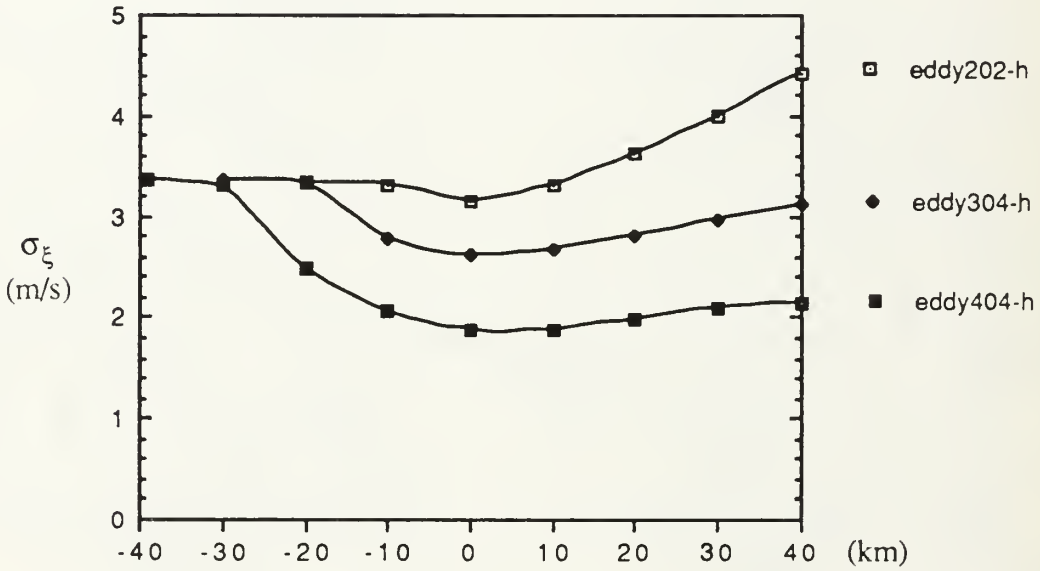

Figure 4-18: Square Root of Spatial Average Square Error vs. Horizontal Correlation Length Uncertainty.

It is interesting to note that, for assumed horizontal correlation lengths of L_x and L_y both equal to 1 km*, the error is 3.4 m/s for all the three cases estimated. Furthermore, σ_ξ is less sensitive to a positive correlation length uncertainty than

---

* Correlation length of zero implies no *a priori* information. Our software does not permit the use of zero correlation length, so we used correlation length of 1 km to approximate the case of no *a priori* information.

to a negative correlation length uncertainty when the actual ocean correlation length is long (e.g. longer than 20 km, see the curves associated with ocean fields Eddy304 and Eddy404), while it is more sensitive to a positive uncertainty than to a negative uncertainty when the actual correlation length is short (e.g. 20 km, see the curve associate with Eddy204).

In an ocean with small eddies, Figure 4-18 suggests that using a correlation length longer than the actual one could result in a large increase of estimate error. Whether or not the estimate is sensitive to an inexact and longer correlation length used really depends on the resolution of the system. We see from Figure 4-10 that the minimum horizontal resolution length of the Greenland Sea array is approximately 30 km, almost regardless of what the correlation length of the field is. This implies that the array is unable to resolve ocean features smaller than 30 km. In other words, an ocean field with a correlation length shorter than 30 km (e.g. 20 km) can not be monitored adequately. In that case any additional *a priori* information, even though wrong, is totally absorbed by the estimator for solution construction, thus leading to an uncertainty sensitive estimate. In contrast, for an ocean field with a correlation length longer than 30 km, the array turns into an adequate system. The corresponding estimator now has the ability to reject extraneous information. The result is an uncertainty insensitive estimate.

TABLE 4-2 shows the value of σ_ξ for each suboptimal estimate, as well as the percent difference in σ_ξ between each suboptimal estimate and the optimal estimate for the ocean field Eddy404. By selecting a value for the maximum acceptable percent difference in σ_ξ between the suboptimal estimators and the optimal estimator, we can compute from the curves in Figure 4-18 the maximum

allowable uncertainty in correlation length. TABLE 4-3 shows, for each simulated field, the allowable range of uncertainty in correlation length if the difference between σ_ξ for the suboptimal and optimal estimators is not to exceed ten percent.

TABLE 4-2 : THE ESTIMATE ERROR AND % DIFFERENCE TO THE OPTIMAL ESTIMATE FOR EDDY404.

ΔL_x, ΔL_y (km)	σ_ξ	% difference
-30	3.30	75.53
-20	2.50	32.98
-10	2.06	9.57
10	1.88	0.00
20	1.99	9.63
30	2.10	11.70

TABLE 4-3 : TEN % DIFFERENCE ALLOWABLE UNCERTAINTY RANGE.

L_x, L_y (km)	Allowable ΔL_x and ΔL_y Range (km)
20 km	-20.0 ~ 15.6
30 km	-11.8 ~ 23.7
40 km	-10.4 ~ 25.8

TABLE 4-3 quantitatively confirms our earlier observation from Figure 4-18 that the estimate error is less sensitive to a positive uncertainty in correlation length than to a negative one in ocean volumes containing large structures, and the result is reversed for an ocean volume containing small structures.

V. CONCLUSION

A. ESTIMATOR PERFORMANCE

In order to obtain a unique estimate of the sound speed perturbation field, *a priori* information in the form of a sound speed perturbation covariance matrix is used in the Gauss-Markoff estimator. As discussed in Chapter 4, given that the sound speed perturbation field has a gaussian shape correlation, the *optimal estimate* for the field is obtained when the *assumed* correlation length (*i.e.*, the correlation length used to calculate the input covariance matrix $C_{\underline{\delta c}}$) is equal to the *actual* correlation length present in the ocean. A primary goal of this thesis is to evaluate the effect on our estimator when the assumed correlation length is *not* equal to the actual one. As this happens, the estimate becomes *suboptimal.* When the actual correlation length is not exactly known, it has been suggested by Cornuelle (1985) and Chiu (1987) to use a conservative assumption (*i.e.*, a small correlation length) so as not to "assume too much" about the sound speed perturbation field.

From our simulation study we found that the optimal estimate for the sound speed perturbation field typically has an RMS error between 1 and 2 m/s (i.e., 20% to 40% comparing to the 5 m/s signal level). For the suboptimal case, the estimate is actually less sensitive to a positive correlation length uncertainty (*i.e.*, the assumed correlation length is longer than the actual one) than to a negative uncertainty when the actual correlation length is longer than 30 km. On the other hand, when the actual correlation length is shorter than 30 km (for example 20 km) the estimate becomes *more* sensitive to a positive uncertainty

than to a negative uncertainty. The reason for this switching of behavior at a correlation length of 30 km has something to do with the resolution of the Greenland Sea array. In our resolution analysis we found that the Greenland Sea array has a resolution length of about 30 km. Therefore, for an ocean field with a correlation length small than 30 km (for example 20 km), the use of a correlation length longer than the actual one for inversion would ingest extraneous information into an information hungry estimator. This estimator basically accepts all the wrong information. It is thus preferable to be conservative and use a correlation length which is likely to have a negative uncertainty when the system resolution is inadequate for measuring the expected scale. On the other hands, if we know from resolution analysis that the resolution is adequate for a particular ocean region, a positive correlation length uncertainty is acceptable in this case.

By specifying the maximum acceptable percent difference in σ_ξ (which is essentially a spatial average of local estimate errors) between the suboptimal and optimal estimators, we arrive at one possible criterion for designing the estimator. If this difference, in the case of an expected ocean correlation length of about 40 km, is required to be less than ten percent (for example), the estimator can tolerate any correlation length uncertainty between -10.4 and 25.8 km, a spread of 35.6 km.

We have also shown that a higher noise level results in basically unchanged RMS error and resolution. This result suggests that the estimate error is not dominated by the random error, but rather by the bias error arising from the fact that the tomography problem is underdetermined. This insensitivity to

random noise is one benefit of using a Gauss-Markoff estimator, which always tries to minimize the effect of random noise (Chiu *et al*, 1987).

The failure of array elements has a very pronounced effect on the RMS error and resolution, especially if two elements fail. The comparison of cases simulating the failure of one or more elements indicates that the RMS error becomes very large and resolution becomes very poor in areas that no longer have rays passing through them. However, in regions still containing acoustic rays, the RMS error is only 25% higher than that of the full array case.

B. RECOMMENDATIONS FOR FUTURE IMPROVEMENT

All numerical simulations were performed on a DEC MicroVAX. Each run required roughly five and one-half hours of CPU time. A machine of greater computational power and larger memory size would allow us to divide the ocean volume into finer spatial meshes for improved analysis.

We can derive statistical information concerning the vertical ocean structure from historical data using the *empirical orthogonal function* (EOF) approach of Cornuelle (1983, pp. 139). EOF analysis has been widely applied in research fields other than tomography. In EOF analysis, the vertical structure of the ocean is represented by a set of orthogonal vectors. These vectors can be derived from a singular value decomposition of a matrix containing historical data from hydrographic surveys. The EOF method gives *a priori* information about the vertical structure which is more realistic than that provided by the Gaussian shape correlation used in this study, and is recommended for use when the actual tomographic data from the Greenland Sea Project become available.

REFERENCES

Backus, G.E. and Gilbert, J.F., "Numerical Applications of a Formalism for Geophysical Inverse Problems", *Geophys. J. R. Astron. Soc.*, Vol. 13, pp. 247-76, 1967.

Bushong, P.J., "Tomographic Measurements of Bartropic Motion", Engineer's Thesis, MIT/WHOI Joint Program, Cambridge and Woods Hole, MA, 1978.

Chiu, C.S., Lynch, J.F., and Johannessen, O.M., "Tomographic Resolution of Mesoscale Eddies in the MIZ - A Preliminary Study", *Journal of Geophysical Research*, Vol. 92, No. C7, pp. 6886-6902, Jun. 1987.

Chiu, C.S. and Desaubies, Y., "A planetary wave analysis using the acoustic and conventional arrays in the 1981 Ocean Tomography Experiment", *Journal of Physical Oceanography*, Vol 17, No. 8, pp.1270-1287, 1987.

Cornuelle, B.D., "Inverse methods and results from the 1981 Ocean Acoustic Tomography Experiment", Ph.D. dissertation, MIT/WHOI, 1983.

Cornuelle, B.D. and Collaborators, "Tomographic maps of the ocean mesoscale. Part 1: Pure Acoustics", *Journal of Physical Oceanography*, Vol. 15, pp. 133-152, Feb. 1985.

DeFerrari, H.A. and Nguyen, H.B., "Acoustic Reciprocal Transmission Experiment, Florida Straits", *The Journal of the Acoustical Society of America*, Vol 79, pp. 299-315, 1986.

Gerald, C.F., *Applied Numerical Analysis*, 4th ed., Addison Wesley, Inc., 1989.

Greenland Sea Science Planning Group, *Greenland Sea Project - An International Plan of the Arctic Ocean Sciences Board*, Jan. 1986.

Howe B.M. and Worcester P.E., "Ocean acoustic Tomography: Mesoscale Velocity", *J. Geophys. Res.* Vol. 94, No. C4, pp. 3785-3805. 1987.

Kinsler, L.E., Frey A.R., Coppens, A.B., and Sanders, J.V., *Fundamentals of Acoustics*, 3rd ed., John Wiley & Sons, 1982.

Liebelt, P.B., *An Introduction To Optimal Estimation*, Addison Wesley, Inc., 1967.

Lynch, J.F., Spindel, R.C., Chiu, C.H., Miller J.H., and Birdsall, T.G., "Results from the 1984 Marginal Ice Zone Experiment Preliminary Tomography Transmissions: Implications for Marginal Ice Zone, Arctic, and Surface Wave Tomography", *J. Geophys. Res.*, Vol. 92, No. C7, pp. 6869-6885, 1987.

Miller, J.H., Lynch, J.F., and Chiu, C.S., "Estimation of Sea Surface Spectra using Acoustic Tomography", *The Journal of the Acoustical Society of America*", Vol. 86, No. 1, pp. 326-345, Jul. 1989.

Menke, W., *Geophysical Data Analysis: Discrete Theory*, Academic Press, Inc., 1984.

Munk, W. and Wunsch, C., "Ocean Acoustic Tomography: A Scheme for Large Scale Monitoring", *Deep-Sea Research*, Vol. 26A, pp. 123-161, 1979.

Richard, P.F., *Coordinate Conversion for Hydrographic Surveying*, National Charting Research and Development Laboratory, Dec. 1985.

Stoughton, R.B., Flatte, S.M. and Howe, B.M., "Acoustic Measurements of Internal Wave Rms Displacement and Rms Horizontal Current off Bermuda in Late 1983", *J. Geophys. Res.*, Vol. 91, No. C6, pp. 7721-7731, 1986.

The Ocean Tomography Group, "A Demonstration of Ocean Acoustic Tomography", *Nature*, Vol. 299, pp. 121-125, 1982.

Uginčius, P., "Ray Acoustic and Fermat's Principal in a Moving Inhomogeneous Medium", *The Journal of the Acoustical Society of America*, Vol 51, No. 5, pp. 1759-1763, Jun. 1970.

Worcester, P.E. and Howe, B.M., *GSP88/MST88: Deployment Cruise Summary*, Feb. 1989.

Ziomek, L. J., *Underwater Acoustics A Linear Systems Theory Approach*, Academic Press, Inc., 1985.

INITIAL DISTRIBUTION LIST

	No. Copies
1. Defense Technical Information Center Cameron Station Alexandria, VA 22304-6145	2
2. Library, Code 0142 Naval Postgraduate School Monterey, CA 93943-5002	2
3. Prof. Ching-Sang Chiu, Code 68Ci Department of Oceanography Naval Postgraduate School Monterey, CA 93943	20
4. Prof. James H. Miller, Code 62Mr Department of Electrical and Computer Engineering Naval Postgraduate School Monterey, CA 93943	4
5. Prof. Anthony A. Atchley, Code 61Ay Department of Physics Naval Postgraduate School Monterey, CA 93943	1
6. CDR Kurt V. Schnebele, Code 68Sn Department of Oceanography Naval Postgraduate School Monterey, CA 93943	1
7. Dr. Yao, Neng-Chun P.O. Box 90151-24 Taipei, Taiwan Republic of China	1
8. Director Tu Chinese Naval Hydrographic and Oceanographic Office Tsoying, Kaohsiung, Taiwan Republic of China	1

9. Library of Chinese Naval Hydrographic and Oceanographic Office 1
Chinese Naval Hydrographic and Oceanographic Office
Tsoying, Kaohsiung, Taiwan
Republic of China

6. LT Kim, Jong Pok 1
SMC #2529
Naval Postgraduate School
Monterey, CA 93943

10. LT Kao, Chih-Chung 5
31, 7 Alley, 546 Lane, 1st Sec., Yen-Ping Rd.,
Shin-Chu, Taiwan
Republic of China

Thesis
K142385 Kao
c.1 A study of the sensitivity of the Greenland Sea acoustic tomography array.

Thesis
K142385 Kao
c.1 A study of the sensitivity of the Greenland Sea acoustic tomography array.

A study of the sensitivity of the Greenl

3 2768 000 88928 1
DUDLEY KNOX LIBRARY